ASSESSING DT-MRI TRACTOGRAPHY RESULTS VIA

SAMPLING THE FIBER TRACT SPACE

by

Ahmet Burak Yoldemir

B.S., in Electrical and Electronics Engineering, Boğaziçi University, 2009

Submitted to the Institute for Graduate Studies in

Science and Engineering in partial fulfillment of

the requirements for the degree of

Master of Science

Graduate Program in Electrical and Electronics Engineering

Boğaziçi University

2011

ASSESSING DT-MRI TRACTOGRAPHY RESULTS VIA

SAMPLING THE FIBER TRACT SPACE

APPROVED BY:

Assoc. Prof. Burak Acar . . . .

(Thesis Supervisor)

Assoc. Prof. Murat Saraçlar . . . .

Assist. Prof. Mehmet Burçin Ünlü . . . .

DATE OF APPROVAL: 06.06.2011

ACKNOWLEDGEMENTS

ABSTRACT

ASSESSING DT-MRI TRACTOGRAPHY RESULTS VIA SAMPLING THE FIBER TRACT SPACE

Complex neural processes in human brain are realized through a huge number of connections between neural cells. White matter tractography is the only available tool to reconstruct these anatomical connectivities non-invasively and *in vivo*. Following the emergence of diffusion imaging, several tractography algorithms have been proposed, where the local direction of white matter fiber bundles is estimated from measurements of water diffusion in human brain.

The goal of this thesis is to introduce a generic tractography assessment and improvement method for diffusion tensor imaging (DTI) data. The proposed method takes a set of fiber tracts that are generated with any tractography algorithm as the input, and allow the user to interactively assess tractography results by identifying the erroneous or indefinite regions in the DTI data along input tracts and highlighting possible branching patterns of fiber bundles. By introducing alternative pathways that might have been missed by the initial tractography, given tractography results can also be improved.

The technique relies on splitting the input tracts into shorter segments to prevent error accumulation, followed by sampling from the space of short tract clusters to estimate the connectivities between these short fiber segments. After the connectivity values are computed, given a set of seed tracts and a connectivity threshold, the method displays the short tracts that are connected to the seed tracts with a probability higher than the given threshold in an interactive environment. Thus, the possible pathways can be investigated as a function of the connectivity threshold, highlighting the uncertainty in DTI data.

ÖZET

FİBER YOLAK UZAYININ ÖRNEKLENMESİ İLE FİBER TRAKTOGRAFİ SONUÇLARININ DEĞERLENDİRİLMESİ

Beyindeki karmaşık sinirsel süreçler, sinir hücreleri arasındaki çok sayıdaki bağlantı sayesinde mümkün olmaktadır. Beyaz cevher traktografisi, beyindeki bu anatomik bağlantıların canlı içinde müdahalesiz bulunmasında kullanılabilecek tek yöntemdir. Difüzyon görüntülemenin ortaya çıkışını takiben, birçok traktografi yöntemi önerilmiştir. Bu yöntemler, beyaz cevher yolaklarının yönlerini, beyindeki su moleküllerinin difüzyonunun ölçülmesine dayanarak bulmaktadırlar.

Bu tezin amacı, difüzyon tensör görüntüleme verisi üzerinde traktografi sonuçlarının değerlendirilmesi ve geliştirilmesinde kullanılabilecek jenerik bir yöntem ortaya koymaktır. Bu tezde önerilen yöntem, herhangi bir traktografi metodu ile elde edilmiş bir yolak kümesini girdi olarak alır. Bu yolak kümesi içindeki hatalı veya belirsiz bölgeleri teşhis ederek ve yolakların olası dallanmalarını öne çıkararak kullanıcıya sonuçları etkileşimli olarak irdeleme imkanı sunar. Ayrıca, alternatif yolaklar ortaya koyarak traktografi sonuçlarında bulunamamış olan bağlantıları tespit etmek suretiyle verili traktografi sonuçlarını geliştirme olanağı sağlar.

Önerilen teknikte, öncelikle, hata birikimini önlemek amacıyla verili yolaklar kısa parçalara bölünür. Daha sonra, kısa yolak kümelerinin uzayında örnekleme yapılarak kısa yolak çiftlerinin birbirlerine bağlı olma ihtimalleri hesaplanır. Bu ihtimaller hesaplandıktan sonra kullanıcı tarafından belirlenen kısa yolaklara, yine kullanıcı tarafından belirlenen güvenilirlik eşiğinin üzerinde bir olasılıkla bağlı diğer kısa yolaklar etkileşimli bir arayüzle görüntülenir. Böylelikle kullanıcı, verideki belirsizlikler vurgulanacak şekilde, olası yolakları güvenilirlik eşiğinin bir fonksiyonu olarak inceleyebilir.

TABLE OF CONTENTS

LIST OF FIGURES

LIST OF TABLES

LIST OF SYMBOLS

B_i^k	k^{th} bootstrap cluster with S_i being the seed short tract
C_i^k	k^{th} short tract cluster with S_i being the seed short tract
$\mathbf{d}_{ij}$	Bridge vector connecting neighbouring short tracts S_i and S_j
D	Diffusion coefficient
$\mathbf{D}$	A generic diffusion tensor
$\mathbf{D}_i$	The diffusion tensor at the connected end-point of the ith short tract
$\mathbf{H}$	2D short tract connectivity histogram
J_{ij}	Weight of the bridge connecting neighbouring short tracts S_i and S_j
K	Number of cluster samples
L_{ij}	Collinearity of S_i and S_j
N	Number of DWI measurements
P_{ij}	Probability that S_i and S_j are connected
r	Neighbourhood radius
$\mathbf{r}$	Displacement vector
$\mathbf{r}(s)$	Fiber trajectory parameterized by the arc length
R	Number of bootstrap clusters
SI	Signal intensity
S_i	i^{th} short tract
T	Connectivity threshold
$\mathbf{v}_i$	i^{th} short tract's 3D orientation vector
$\mathbf{v}_{in}$	Direction of previous tractography step
$\mathbf{v}_{out}$	Direction of next tractography step
$\widehat{\mathbf{v}}_i$	i^{th} eigenvector of the diffusion tensor
Δ	Voxel size
λ_i	i^{th} eigenvalue of the diffusion tensor
$\bar{\lambda}$	Average eigenvalue of the diffusion tensor

$\mathcal{K}_{ij}$	Collision probability of two diffusing particles originating from two points with $\mathbf{D}_i$ and $\mathbf{D}_j$ respectively
$\mathcal{N}_i$	i^{th} short tract's connected end-point neighbourhood
τ	Diffusion time scaling factor

LIST OF ABBREVIATIONS

2D	Two dimensional
3D	Three dimensional
DTI	Diffusion tensor imaging
DT-MRI	Diffusion tensor magnetic resonance imaging
DWI	Diffusion weighted imaging
EPI	Echo planar imaging
FA	Fractional anisotropy
fMRI	Functional magnetic resonance imaging
FP	False positive
MRI	Magnetic resonance imaging
PDD	Principal diffusion direction
PDF	Probability density function
RA	Relative anisotropy
RK4	4th order Runge-Kutta integration
ROI	Region of interest
SN	Sensitivity
SNR	Signal-to-noise ratio
VR	Volume ratio

1. INTRODUCTION

Diffusion tensor magnetic resonance imaging (DT-MRI or DTI) is widely used to study white matter architecture since its introduction in 1994 [1]. Broadly speaking, diffusion MRI measures the translational displacement of water molecules. It was shown that the water diffusion along white matter fibers are much faster compared to the diffusion perpendicular to them [1–3]. Having this difference between diffusion rates along different directions (i.e., diffusion anisotropy) as a basis, DTI is able to quantitatively describe white matter connectivity in human brain without the use of contrast agents [4].

Tractography is a method to localize the anatomical connections in human brain *in vivo* using diffusion imaging. The major clinical application of tractography is presurgical planning. In most of the patients with brain tumors or lesions, white matter tracts are displaced or distorted. Using tractography, the fiber tracts that are related to vital neural connections can be identified and hence can be preserved during surgical procedures. DTI is also explored as a research tool to study white matter abnormalities in neurological, developmental and psychiatric disorders [4–8], especially in multiple sclerosis, amyotrophic lateral sclerosis, stroke, schizophrenia and reading disability [9].

The proposed method in this thesis provides a user interactive framework for the assessment and improvement of given tractography results based on short tract clustering, which is initially proposed in [10]. The method relies on splitting given fiber tracts to generate shorter and more reliable (less error accumulating) tract segments throughout the brain, followed by an estimation of pairwise connectivities of these short tracts by sampling from the space of short tract clusters. The estimated connectivities (i.e., the probability that two short tracts are on the same long tract bundle) are used to select and display the short tracts that are connected to a given set of seed tracts with a probability higher than the user set threshold in an interactive environment. Thus, the user can identify the unreliable segments/regions in the DTI data along given tracts,

see possible branching patterns of fiber bundles, assess the branching probabilities (as determined by the DTI tensor data) via setting the connectivity threshold and interactively construct new tract bundles that might have been missed by the initial tractography. The ultimate goal is to present the connectivity information embedded in DTI data without bias and in an interactive framework.

This thesis is organized as follows. In Chapter 2, the background information on the anatomy of human brain and DTI are provided. Chapter 3 is reserved for the theoretical details of the proposed tractography assessment method. Chapter 4 presents the evaluation methodology, experimental results and the significance of the findings. In Chapter 5, conclusions of the thesis are drawn and future research directions are proposed.

2. BACKGROUND

2.1. Anatomy of Neural White Matter

Human brain consists of billions of neurons. Each neuron has a cell body, with axon and dendrites extending from it, as shown in Figure 2.1. While the function of axons is to transmit signals among neurons, dendrites receive signals from other axons. Generally, the signal transmission distance is long, hence the axons are myelinated to speed up the signal transmission process. The abundance of myelinated axons in white matter is what gives its white color. To transmit information from one part of the brain to another, hundreds of axons within white matter group together in parallel, thereby forming fiber bundles [11]. Figure 2.2 shows the dissection of white matter, where the fibrous nature of white matter is clearly visible.
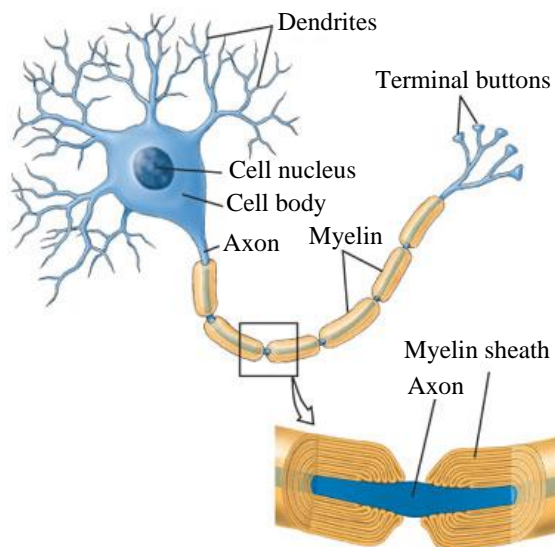
Figure 2.1. A typical myelinated neuron [12].

2.2. Diffusion Tensor Imaging

The rate of diffusion within brain varies with direction due to the presence of physical constraints that obstruct diffusion. It is assumed that, in human brain, main constraint of diffusion is the myelin sheath that surrounds the axons. DTI data describe

Figure 2.2. Brain dissection showing the structure of white matter [13].

the diffusion profile of water within every voxel in brain using a diffusion tensor, which indirectly provides information about fiber tract orientation. Visually, these tensors can be modeled as diffusion ellipsoids with the diffusion tensor eigenvectors corresponding to the principal axes and the eigenvalues to the size in the relevant direction. A diffusion ellipsoid is actually an isoprobability surface that summarizes the mean distance from the ellipsoid center that a water molecule will travel in a certain diffusion time. In regions of brain exhibiting isotropic diffusion, the diffusion profiles result in spherical ellipsoids. Conversely, when anisotropic diffusion is present, more eccentric ellipsoids are observed.

A tensor of order n in 3D space is a mathematical object which is described by 3^n numbers in any given three dimensional coordinate system [14]. A diffusion tensor is a second order tensor in 3D space that represents the macro view of the diffusion process within the corresponding voxel. It corresponds to the inverse covariance matrix of the zero mean 3D Gaussian distribution of the positions of diffusing particles as

$$P(\mathbf{r}) = \frac{1}{\sqrt{|\mathbf{D}|(4\pi\tau)^3}} \exp\left(-\frac{\mathbf{r}^T \mathbf{D}^{-1} \mathbf{r}}{4\tau}\right) \tag{2.1}$$

where $\mathbf{D}$ is the diffusion tensor, τ is the effective diffusion time, and $\mathbf{r}$ is the displace-

ment vector [15]. The diffusion tensor is a 3×3 symmetric, positive semi-definite, second-order tensor.

$$\mathbf{D} = \begin{bmatrix} D_{xx} & D_{xy} & D_{xz} \\ D_{xy} & D_{yy} & D_{yz} \\ D_{xz} & D_{yz} & D_{zz} \end{bmatrix} \tag{2.2}$$

The diffusion tensors are constructed from diffusion weighted imaging (DWI) data of the same volume captured using at least six linearly independent diffusion sensitizing gradient B-fields and one reference non-diffusion sensitized image obtained in the absence of gradient B-fields. DWI data acquired for a specific direction provide information regarding the magnitude of diffusion in the corresponding direction through MR signal attenuation due to out-of-phase spins within a voxel. The amount of signal attenuation depends on the strength and duration of the magnetic field gradient, b, and the diffusion coefficient, D. Signal intensity (SI_1) in homogeneous, systems decreases exponentially as b increases:

$$SI_1 = SI_0 \exp(-bD) \tag{2.3}$$

where SI_0 is the signal intensity without the diffusion sensitizing gradients. b value given above is for a gradient B-field in a single direction. In DTI, gradient fields in several directions are applied simultaneously. In this case, b value is replaced by a 3×3 $\mathbf{b}$ matrix, consisting of 6 distinct terms: b_{xx}, b_{yy}, b_{zz}, $b_{xy} = b_{yx}$, $b_{xz} = b_{zx}$, and $b_{yz} = b_{zy}$ [16]. As stated above, the diffusion tensors can be calculated from DWI data collected with diffusion sensitizing gradient B-fields in six or more directions and one or more reference images. Assume that there are a total of N measurements. Then, 6 distinct elements of the diffusion tensor at a given voxel can be calculated from the DWI intensity values and the elements of the b matrices by solving the following linear

system of equations [17]:

$$\begin{bmatrix} \ln(S_1) \\ \vdots \\ \ln(S_N) \end{bmatrix} = \begin{bmatrix} A_1 \\ \vdots \\ A_N \end{bmatrix} \qquad (2.4)$$

where A_i, $i = 1, \ldots, N$ is defined as

$$A_i = -b_{xxi}D_{xx} - b_{yyi}D_{yy} - b_{zzi}D_{zz} - 2b_{xyi}D_{xy} - 2b_{xzi}D_{xz} - 2b_{yzi}D_{yz} + \ln(S_0). \quad (2.5)$$

Diagonalizing the diffusion tensor results in a set of three eigenvectors $\widehat{\mathbf{v}}_1$, $\widehat{\mathbf{v}}_2$, $\widehat{\mathbf{v}}_3$ with associated eigenvalues λ_1, λ_2, λ_3 listed in decreasing order.

$$\mathbf{D} = \begin{bmatrix} D_{xx} & D_{xy} & D_{xz} \\ D_{xy} & D_{yy} & D_{yz} \\ D_{xz} & D_{yz} & D_{zz} \end{bmatrix} = \begin{bmatrix} \widehat{\mathbf{v}}_1 & \widehat{\mathbf{v}}_2 & \widehat{\mathbf{v}}_3 \end{bmatrix} \begin{bmatrix} \lambda_1 & 0 & 0 \\ 0 & \lambda_2 & 0 \\ 0 & 0 & \lambda_3 \end{bmatrix} \begin{bmatrix} \widehat{\mathbf{v}}_1^T \\ \widehat{\mathbf{v}}_2^T \\ \widehat{\mathbf{v}}_3^T \end{bmatrix} \qquad (2.6)$$

$\widehat{\mathbf{v}}_1$, which is the eigenvector corresponding to the largest eigenvalue is called the principal diffusion direction (PDD). As the tensor is positive semi-definite, the eigenvalues are non-negative, which allows the ellipsoid to be physically realizable [18]. The analogy between the diffusion tensor and the diffusion ellipsoid becomes evident when viewed graphically as in Figure 2.3.

For many applications, the diffusion tensor $\mathbf{D}$ contains too much information, and only a rough estimate of the amount of anisotropy is sufficient. Extracting such an anisotropy index from the diffusion tensor is also very beneficial for comparing different subjects and for monitoring changes over time [16]. As the parameters of the diffusion tensor are sensitive to changes in the orientation of the object that is being scanned, clinical studies tend to use orientation-invariant statistics extracted from diffusion tensors. Such statistics are calculated using combinations of the terms of the diagonalized diffusion tensor, i.e., λ_1, λ_2 and λ_3. The most commonly used anisotropy indices are fractional anisotropy (FA), relative anisotropy (RA) and volume
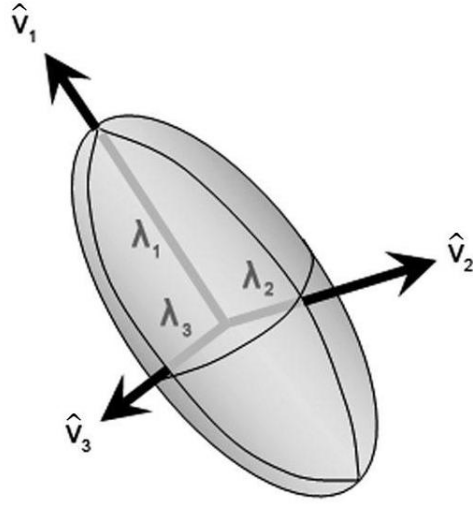
Figure 2.3. The diffusion ellipsoid characterized by 3 eigenvectors and 3 eigenvalues [19].

ratio (VR), defined respectively as

$$FA = \frac{\sqrt{3}}{\sqrt{2}} \frac{\sqrt{\left(\lambda_1 - \bar{\lambda}\right)^2 + \left(\lambda_2 - \bar{\lambda}\right)^2 + \left(\lambda_3 - \bar{\lambda}\right)^2}}{\sqrt{\lambda_1^2 + \lambda_2^2 + \lambda_3^2}} \tag{2.7}$$

$$RA = \frac{\sqrt{\left(\lambda_1 - \bar{\lambda}\right)^2 + \left(\lambda_2 - \bar{\lambda}\right)^2 + \left(\lambda_3 - \bar{\lambda}\right)^2}}{\sqrt{3\bar{\lambda}^2}} \tag{2.8}$$

$$VR = \frac{\lambda_1 \lambda_2 \lambda_3}{\bar{\lambda}^3} \tag{2.9}$$

where

$$\bar{\lambda} = \frac{\lambda_1 + \lambda_2 + \lambda_3}{3}. \tag{2.10}$$

FA is the "magnitude" of $\mathbf{D}$ that can be ascribed to anisotropic diffusion, and it varies between zero (perfectly isotropic diffusion) to one (perfectly anisotropic diffusion). RA is the ratio of the anisotropic part of $\mathbf{D}$ to its isotropic part, and it varies between zero (perfectly isotropic diffusion) to $\sqrt{2}$ (perfectly anisotropic diffusion). Fi-

nally, VR is the ratio of the ellipsoid volume to the volume of a sphere of radius $\bar{\lambda}$, and it varies between one (perfectly isotropic diffusion) to zero (perfectly anisotropic diffusion) [20]. Among these anisotropy indices, FA is the most popular, as some people have a sense of the expected FA values in different brain regions and as they wish to be consistent with older published data for comparative purposes [16]. It is known that, if the FA value is sufficiently high, which implies highly anisotropic diffusion, PDD is a good estimate of the local fiber orientation [21].

It is of utmost importance to understand the limitations and content of DTI data in order to develop adequate analysis and visualization methods. DTI tensor field is a second-order approximation to the underlying diffusion process that is estimated through MR signal attenuation due to out-of-phase spins within a voxel. The size of the voxels cannot be made arbitrarily small because *i)* we need to observe the signal attenuation, *ii)* the anisotropic diffusion pattern in restricted media (fibers) is observable only if the voxel size is larger than the fiber cross section. This imposes a fundamental limitation on the spatial resolution of DTI, prohibiting reconstruction of single fibers. This limitation is most critical at problematic regions such as crossing, kissing fibers (bundles) where the anisotropy of the diffusion tensors are degraded due to (within voxel) averaging [13, 22].

2.3. Literature Review of DTI Tractography

In DTI data, there is uncertainty caused both by the noise and artifacts present in any MR scan, and also by the incomplete modeling of the diffusion signal by a second order tensor. The deterministic tractography methods disregard this inherent uncertainty in the data, and reconstruct fiber tracts by generally drawing paths in vector fields primarily based on PDDs. The probabilistic methods, on the other hand, attempt to take uncertainty stemming from noise and diffusion model imperfections into account. The following subsections elaborate on these two main approaches.

2.3.1. Deterministic Tractography

Deterministic tractography methods compute a single fiber trajectory for every seed point. Result of tractography for a given seed point is a tract connecting two discrete regions of the brain. Among these methods, streamline techniques rely on bidirectionally following the PDD at every point in the brain [22–26]. In these methods, a white matter fiber tract trajectory is represented as a 3D space curve, i.e., $\mathbf{r}(s)$, parameterized by the arc length, s, of the trajectory. Following the assumption that the principal eigenvector, $\mathbf{v}_1$, lies parallel to the local fiber tract direction, the fiber trajectory is reconstructed by solving the implicit differential equation

$$\frac{d\mathbf{r}(s)}{ds} = \mathbf{v}_1(\mathbf{r}(s)) \tag{2.11}$$

using a numerical integration scheme such as the Euler's method or the Runge-Kutta method. These methods do not exploit the whole information in the diffusion tensor.

Tensorline methods, on the other hand, use the entire diffusion tensor to deflect the incoming vector direction to determine the direction of the new step [27, 28] as

$$\mathbf{v}_{out} = \mathbf{D} \cdot \mathbf{v}_{in} \tag{2.12}$$

where $\mathbf{v}_{in}$ represents the propagation direction from the previous integration step and $\mathbf{v}_{out}$ is the direction of the next step. This limits the curvature of the deflection, thereby smoothing the reconstructed fiber trajectories. The reader is referred to [27] for a quantitative evaluation of the performance of streamline and tensorline methods. Figure 2.4 shows a comparison of streamline (the Euler's method) and tensorline techniques for fibers of the internal capsule.

The deterministic approaches have the advantages of speed and simplicity. However, they also have severe limitations. As the decisions are made on local scales, entire space of possible fiber tract trajectories may not be fully explored. Moreover, there is an inherent uncertainty in diffusion tensor elements due to the nature of DTI (note
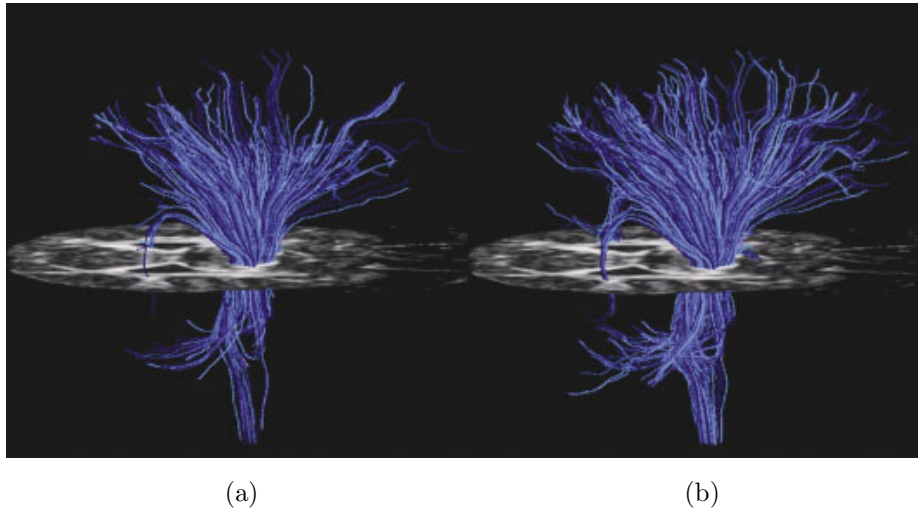
Figure 2.4. Comparison of deterministic techniques for tracking fibers of the internal capsule within human brain (a) Streamline tracking (b) Tensorline tracking [27].

that the data represent a 3D zero mean Gaussian distribution). Hence, algorithms that rely on stepwise propagation, like streamline and tensorline methods, accumulate error along the fiber paths.

To account for the noise and uncertainty in DTI data, explicit and implicit regularization methods are widely being employed. In [29], a nonlinear diffusion filter to regularize the PDD vector field is proposed. This filter uses an anisotropic diffusion model, modulated by a PDD vector field regularity map. In [30], Rician statistics are used to improve fiber orientation estimation. Anisotropic filtering to filter DWI data prior to DTI tensor field computation is introduced in [31]. B-spline functions are also used as a regularizing basis [22].

Despite their disadvantages, deterministic algorithms remain as the most commonly used methods in clinical applications [32].

2.3.2. Probabilistic Tractography

The probabilistic tractography methods basically aim at characterizing the uncertainty in the fiber tract trajectory estimates. In these methods, for every seed point, a set of possible fiber tracts are computed. In reconstructing each of these tracts, at

each step, instead of progressing along the PDD, a sample is drawn from the probability distribution function (PDF) for the fiber orientations at the corresponding point and a step is taken in this direction. Proceeding likewise, a fiber tract trajectory is reconstructed, which becomes a sample from the global connectivity distribution. A large number of samples are drawn, and the probability that given two regions are connected is computed by counting the number of tracts that passed through both regions divided by the number of samples drawn.

The main difference between the methods in this class is the modeling of the fiber orientation PDF. In [33], the direction of propagation is perturbed at each step proportional to the anisotropy of the diffusion tensor at the corresponding point. In [34], the uncertainty of the fiber orientations is modeled using the normal distribution, where the parameters were set heuristically. In [35], the PDF for local fiber orientations is rigorously formalized in a Bayesian framework instead of heuristically perturbing the direction of progress. An alternative Bayesian method is presented in [36], where unlike [35], Markov Chain Monte Carlo technique is avoided by a simpler parameter modeling. An extension of [35] is presented in [37], for the case of multiple fiber orientations. In [38], replacing the *ad hoc* PDF models with the Watson distribution is proposed. Similarly, in [39], the step direction is chosen from either a Watson distribution or a Bingham distribution according to the fiber direction uncertainty.

A random walk model to find the connectivities between the brain regions is presented in [40], where only voxel-to-voxel jumps are allowed. This study is based on the idea of a particle that performs a macroscopic random walk through the set of voxels. The probability of a jump in a given direction was chosen to depend monotonously on the diffusion coefficient along the jump direction in the start and target voxel of the jump. The particle then moves with a higher probability along the fiber direction than perpendicular to it. This work is extended to the case where jumps are continuous in [41].

To characterize the uncertainty in fiber tract trajectory estimates without using a PDF model, bootstrap tractography was proposed in [42]. The bootstrap method

is a nonparametric procedure for estimating the statistical properties of a population from a limited number of measurement samples, without prior assumptions about the population distribution. It uses repeated random sampling with replacement from a set of measurements to generate estimates of the underlying statistical distributions of the measurements [43]. In [42], the bootstrap method is used to generate a reliable DTI dataset. To use bootstrap tractography, however, several DTI datasets must be acquired, which considerably increases the imaging time. Number of bootstrap samples to obtain reliable DTI parameters is investigated in [44]. Two alternative bootstrap methods have been proposed to solve the problem of increased imaging time, which are not based on repeated data acquisition: wild bootstrap [45] and residual bootstrap [46]. Yet, concerns have been raised about the applicability of bootstrap to quantify uncertainty in DTI parameters in [47], where it is shown that appropriate use of the wild and repetition bootstrap methods critically depends on the shape of the tensor that is being estimated.

In general, probabilistic methods give a more comprehensive picture of connectivities in the brain and they are also noted to behave more robustly in case of complex intravoxel fiber configurations [35]. However, they are computationally much more demanding compared to the deterministic methods. Moreover, they fail to describe the fiber orientation correctly when the assumed models do not fit the data. They also show a decrease in connection probability with increasing distance from seed point due to the progressive dispersion of streamlines [48]. The outputs of probabilistic methods are generally presented as connectivity maps, which are harder to interpret compared to individual streamlines of deterministic tractography. Figure 2.5 shows typical examples of color coded connectivity maps that shows the frequency of connection to seed points marked with white arrows.
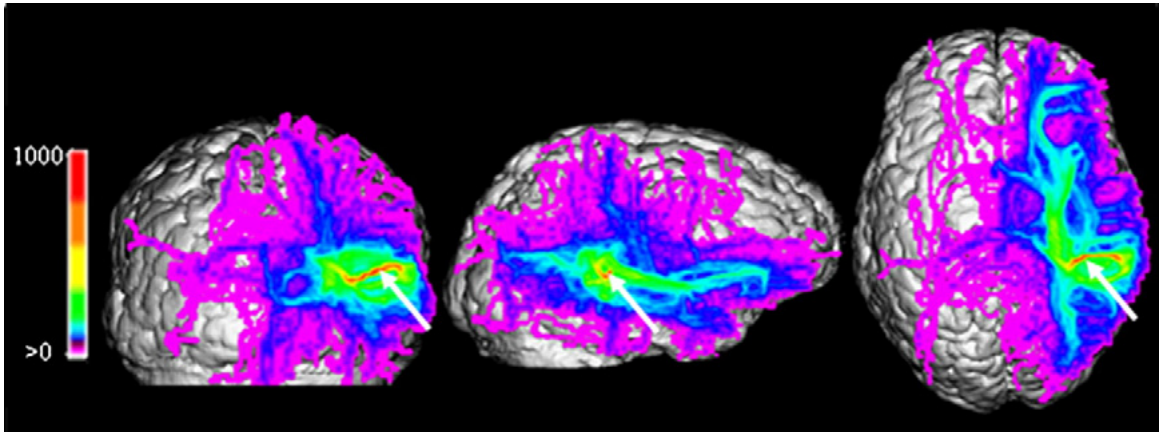
Figure 2.5. Examples of connectivity maps for seed regions marked with arrows [48].

3. FIBER TRACTOGRAPHY ASSESSMENT

3.1. Notation

The proposed method takes a set of long fiber tracts as its input and splits them into shorter tracts, $\{S_i\}$. The subscripts refer to short tract indices. For the sake of simpler notation, the two end-points of a short tract are not explicitly discriminated. The algorithm is based on sampling the space of short fiber tract clusters. The cluster sampling strategy is based on connectivities (bridge weights, J_{ij}) between neighbouring short tracts' (S_i and S_j) closest end-points and respective neighbourhoods ($\mathcal{N}_i$ and $\mathcal{N}_j$) are also defined likewise. The associated diffusion tensors ($\mathbf{D}_i$ and $\mathbf{D}_j$) are the ones at the connected end-points of a short tract pair. Figure 3.1 depicts sample short tracts in a small neighbourhood with definitions of terms used in the rest of this thesis. Table 3.1 provides a summary of the notation used in Chapter 3.

3.2. Generating the Short Fiber Tracts

The proposed method is a generic algorithm that is applicable to any given set of fiber tracts. We have chosen to use the streamline algorithm with 4th order Runge-Kutta (RK4) integration to compute the long input fiber tracts [25]. The Log-Euclidean framework is used for diffusion tensor interpolation at non-integer grid points during tracking [49]. The step size of streamline tractography is half of the length of a voxel's smallest dimension, maximum curvature threshold is 20° and minimum FA threshold is 0.2. Tract computation is initiated from all high FA voxels (FA > 0.2) throughout the volume. The computed long tracts are recursively split into short tracts (S_i , $i = 1, ..., M$) starting from the lowest FA point along each long tract with the constraint of a minimum short tract length of four times the length a voxel's largest dimension. The total number of short tracts, M, is not fixed and is determined by the splitting constraints mentioned above. The rest of the algorithm is based on sampling from the space of clusters of S_i's and estimating pairwise short tract connectivity probabilities (P_{ij} , $i \neq j$, $(i, j) = 1, ..., M$).
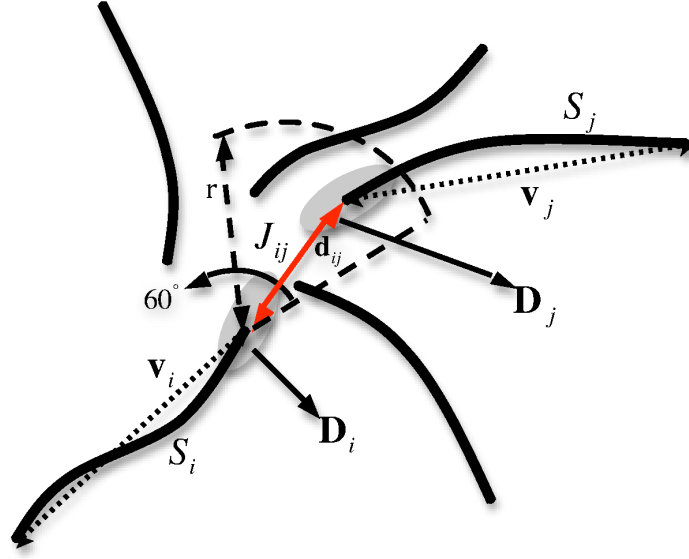
Figure 3.1. Demonstration of the terminology used in Chapter 3.

3.3. Pairwise Short Tract Connectivity Estimation

The principal goal of the proposed algorithm is to estimate the pairwise short tract connectivity probabilities, namely P_{ij}'s. The pursued approach is to sample from the space of short tract clusters and use this sample set to approximate P_{ij}'s as

$$P_{ij} = P(S_i, S_j) = \sum_{m=1}^{M} \sum_{k=1}^{K} P(S_i, S_j | C_m^k) P(C_m^k) \tag{3.1}$$

$$P(S_i, S_j | C_m^k) = \begin{cases} 1, & S_i, S_j \in C_m^k \\ 0, & o.w. \end{cases} \tag{3.2}$$

$$Z \times P(C_m^k) = \min_{i,j} \{J_{ij} | S_i, S_j \in C_m^k\} = w_m^k \tag{3.3}$$

where $P(S_i, S_j | C_m^k)$ represents the connectivity of S_i and S_j given the cluster C_m^k, and $P(C_m^k)$ represents the probability of cluster C_m^k, which is the kth cluster sample for the mth seed short tract. The former probability is modeled based on the membership of the short tracts to the given cluster. The latter probability is modeled to be proportional to the *weakest* bridge's weight (w_m^k) in a given cluster. Z is the unknown scaling factor. Note that J_{ij} is not defined for $S_i, S_j \in C_m^k \land (S_i \notin \mathcal{N}_j \lor S_j \notin \mathcal{N}_i)$, hence not considered

Table 3.1. Summary of notation accompanying Figure 3.1.

Notation	Definition
S_i	i^{th} short tract, $i = 1, ..., M$
$\mathbf{v}_i$	i^{th} short tract's 3D orientation vector
$\mathbf{D}_i$	The diffusion tensor at the connected end-point of the ith short tract
$\mathcal{N}_i$	i^{th} short tract's connected end-point neighbourhood
r	Neighbourhood radius
J_{ij}	Weight of the bridge connecting neighbouring short tracts S_i and S_j
$\mathbf{d}_{ij}$	Bridge vector connecting neighbouring short tracts S_i and S_j
C_i^k	k^{th} short tract cluster with S_i being the seed short tract, $i = 1, ..., K$
P_{ij}	Probability that S_i and S_j are connected

in the *minimum* operator in Equation 3.3. Combining Equations 3.1-3.3, we get

$$Z \times P_{ij} = \sum_{\substack{(m,k) = (1,1) \\ S_i, S_j \in C_m^k}}^{(M,K)} w_m^k = \mathbf{H}(i,j) \tag{3.4}$$

where $\mathbf{H} \in \Re^{M \times M}$ is 2D weighted histogram of short tract co-occurences in the sampled cluster set, M is the total number of short tracts (seed tracts) and K is the number of cluster samples per seed short tract. $\mathbf{H}$ is sparse and symmetric.

The bridge weights, J_{ij}'s, are defined as

$$\mathcal{K}_{ij} = \frac{1}{\sqrt{(2\pi\tau)^3 |\mathbf{D}_i + \mathbf{D}_j|}} \exp\left\{ \frac{-1}{2\tau} \mathbf{d}_{ij}^T (\mathbf{D}_i + \mathbf{D}_j)^{-1} \mathbf{d}_{ij} \right\} \tag{3.5}$$

$$L_{ij} = \left| \cos(\angle(\mathbf{v}_i, \mathbf{v}_j)) \right| \tag{3.6}$$

$$J_{ij} = \mathcal{K}_{ij} \times u\left(L_{ij} - \frac{\sqrt{3}}{2}\right) \times L_{ij} \tag{3.7}$$

where L_{ij} measures the collinearity of S_i and S_j via the angle between their major orientations (See Figure 3.1), $u(\cdot)$ is the unit step function acting as a threshold on collinearity (connected short tracts' orientations are not allowed to deviate more than $30°$), $\mathcal{K}_{ij}$ is the collision probability of two diffusing particles initially at neighbouring short tract end-points and τ is the diffusion time scaling factor set such that $\exp\left\{\frac{-(10\Delta)^2}{2\tau\lambda_{max}}\right\} = 0.01$ to ensure that the computed $\mathcal{K}_{ij}$'s do not die prohibitively fast within the short tract end-point neighbourhood, determined by r. Δ is the voxel size, λ_{max} is the maximum diffusion tensor eigenvalue in the dataset. The exact value of τ is not critical because J_{ij}'s relative values are used, as will be explained below.

3.4. Short Tract Cluster Sampling and Histogram Generation

Sampling the short tract cluster space, that includes all sub-sets of M short tracts, plays a key role in the proposed algorithm. The sampling should concentrate on the high probability regions of the cluster space so that the 2D histogram $\mathbf{H}$ provides a good estimation of pairwise short tract connectivities. The cluster sampling strategy for a given short seed tract S_i is to take K cluster samples from the neighbourhood of the corresponding *base cluster* (C_i^0). C_i^0 is the cluster that corresponds to the input long tract (See Section 3.2) which includes the seed tract S_i as one of its segments. This is repeated for all short tracts taken as the seed tract, generating $K \times M$ clusters (with repetitions).

Figure 3.2 summarizes the cluster sampling in the neighbourhood of C_i^0 that is done by repeatedly breaking C_i^0 into two segments at a randomly selected bridge along C_i^0, random re-building of the broken bridge based on DTI data and completing the rest of the cluster (beyond the re-built bridge) deterministically. The bridge to break is selected among the bridges along C_i^0 with a probability inversely proportional to the bridge weights, $\{J_{uv}|S_u, S_v \in C_i^0\}^1$. Thus, the weaker bridges (i.e., more unreliable points along C_i^0) have higher probability of being broken. Among the two segments of C_i^0 formed, the one which includes the seed tract S_i is retained. A new bridge is formed from the end-point of the retained segment, in place of the broken bridge, to a

---

[1]Note that J_{uv} is not defined for $S_u, S_v \in C_i^0 \wedge (S_u \notin \mathcal{N}_v \vee S_v \notin \mathcal{N}_u)$
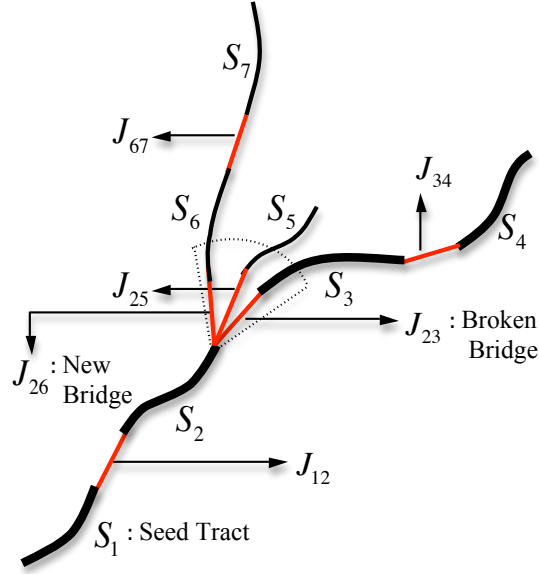
Figure 3.2. Demonstration of the cluster sampling process.

neighbouring short tract end-point with a probability proportional to the corresponding bridge weights. Thus, the stronger bridges (i.e., bridges to the neighbours that are more likely to get connected to the retained cluster segment) have higher probability of being built. The rest of the cluster is formed deterministically by choosing the strongest bridge (i.e., the bridge with the highest weight) among the ones to neighbouring short tracts from the open end of the cluster being built, until an empty short tract end-point neighbourhood is reached.

Figure 3.2 shows an example of the short tract cluster sampling process. In this figure, S_1 is the seed cluster with *base cluster* $C_1^0 = \{S_1, S_2, S_3, S_4\}$. The bridge between S_2 and S_3 was chosen at random to be broken, with probability equal to $J_{23}^{-1}/(J_{12}^{-1} + J_{23}^{-1} + J_{34}^{-1})$. The segment $\{S_1, S_2\}$ is retained. The bridge between S_2 and S_6 was chosen at random to be built, with probability equal to $J_{26}/(J_{26} + J_{25} + J_{23})$. The bridge between S_6 and S_7 was chosen to be built deterministically to complete the new cluster. J_{67} is the maximum among the weights of the bridges connecting the open end of S_6 to its neighbours.

After each new cluster (where cluster repetitions are allowed) C_i^k is created, $\mathbf{H}$ is

updated following Equation 3.4, as

$$\mathbf{H}(u,v) \leftarrow \mathbf{H}(u,v) + w_i^k \ , \ \forall(u,v) \text{ s.t. } S_u, S_v \in C_i^k. \tag{3.8}$$

Approximating any distribution by accumulating samples drawn from that distribution requires that the number of samples is large. Hence, to model the distribution of pairwise connectivities between short tracts accurately, the number of short tract clusters created should be large. However, this operation may be prohibitive in terms of computational cost. For this purpose, we propose to use bootstrap sampling on short tract clusters prior to accumulating the connectivity histogram. Using the bootstrap procedure, a large number of bootstrap clusters can be generated with replacement from a limited set of clusters. A bootstrap cluster is shown as $B_i^r \in \{C_i^0, C_i^1, \ldots, C_i^K\}$, where $r = 1, 2, \ldots, R$ and $R > K$.

Using bootstrap method will obviously introduce a computational advantage as the initial set of clusters may be smaller. However, it should be noted that, bootstrapping will not allow us to explore the whole cluster space beyond the subspace represented by the set of the clusters that are initially generated. It will only allow us to infer more accurate results from that set. In other words, even if the bootstrap method acts like repeating the experiments, one should be aware that the experiments are not actually repeated, but the results of the experiments are more thoroughly assessed.

Depending on the requirements of the application, *bootstrap sampling* may or may not be used under the light of the discussion above. Alternatively, accumulating the histogram directly without bootstrapping, *weighted histogram sampling* can be employed. The pseudo-code in Figure 3.3 summarizes the proposed algorithm using weighted histogram sampling, given a set of long fiber tracts. The algorithm that uses bootstrap sampling is similar, except that, instead of updating the histogram for each C_i^k, B_i^r's are drawn from the set of C_i^k's first, and the histogram is updated using these bootstrap clusters. Bootstrap sampling is unweighted, i.e., probability of drawing a cluster among $\{C_i^0, \cdots, C_i^k\}$ as a bootstrap cluster is the same.

for all *LongTract* ∈ InputLongTractSet **do**

    $\{S\} \leftarrow \{S\} \cup \{\text{Split } LongTract \text{ into short tracts}\}$

end for

$M \leftarrow \# \text{ of } S_i\text{'s}$

for $i = 1 \rightarrow M$ **do**

    for Both end points of S_i **do**

        Find neighbouring short tract end points

        $\{J\} \leftarrow \{J\} \cup \{\text{Compute jump weights } J_{i-}\}$

    end for

end for

for $i = 1 \rightarrow M$ **do**

    Get C_i^0 for the seed tract S_i

    Set $\{J\}_i \subset \{J\}$ s.t. $J_{uv} \in \{J\}_i \Leftrightarrow S_u, S_v \in C_i^0$

    for $k = 1 \rightarrow K$ **do**

        {See Figure 3.2}

        Randomly select $J_{toBreak} \in \{J\}_i$

        Retain the segment of C_i^0 that includes S_i

        Determine potential bridges to be built, $\{J\}_{pot}$

        Randomly select $J_{toBuild} \in \{J\}_{pot}$

        Connect $J_{toBuild}$ and complete C_i^k

        $\mathbf{H}(u,v) \leftarrow \mathbf{H}(u,v) + w_i^k \; \forall (u,v) \text{ s.t. } S_u, S_v \in C_i^k$

    end for

end for

Figure 3.3. The proposed algorithm for a given long fiber tract set.

3.5. Interactive Presentation of the Results

The objective of the proposed algorithm is to answer the following question: *Given a seed short tract, what are the other short tracts that are connected to it with a probability higher than a given threshold?* Specifically, given S_i as the seed tract, we seek the set of short tracts $\{S_j\}_i$, such that $P(S_j|S_i) > T$ where T is the user determined threshold. Following Equation 3.4, $P(S_j|S_i)$ can be estimated as

$$P(S_j|S_i) = \frac{P(S_i, S_j)}{P(S_i)} = \frac{\mathbf{H}(i,j)}{\sum_{j=1}^{M} \mathbf{H}(i,j)}. \tag{3.9}$$

Consequently, the set of short tracts $\{S_j\}_i$ is determined by thresholding the ith row of $\mathbf{H}(i,j)$ after row-wise normalization. The column indices above the threshold T mark the short tracts connected to the seed short tract. Displaying $\{S_j\}_i \cup S_i$ provides an intuitive way to visualize the pathways with branching at uncertain locations. User interaction is achieved via selecting the seed short tracts (all short tracts intersecting a user specified region of interest (ROI) are marked as seed short tracts) and setting T.

Row normalized $\mathbf{H}(i,j)$ is computed once for each data set and saved with the set of short tracts. Setting the seed ROI, the threshold T and marking the short tracts connected to the seed short tracts with a probability above T is performed in real time.

4. EVALUATION AND RESULTS

4.1. Datasets

The algorithm is evaluated quantitatively on phantom DTI data simulating kissing and crossing fibers at different SNR levels, as well as qualitatively on *in vivo* DTI data acquired from a healthy individual.

The phantom DTI data were generated for two geometries, kissing and crossing [50]. The resolution is $0.1 \times 0.1 \times 0.1$ units while the ground truth fibers' diameters are one unit. The noise-free tensors are aligned with the fiber orientation (principal diffusion directions are tangent to the fiber centerline) inside the fibers and have FA = 0.82 with $\lambda_{max} = 0.0016, \lambda_{med} = \lambda_{min} = 0.00025$. The noise-free tensors outside the fibers are randomly oriented and have FA = 0.13 with $\lambda_{max} = 0.001, \lambda_{med} = \lambda_{min} = 0.0008$. Six diffusion weighted MR signals (DWI$_i$'s) are computed by assuming unit base MR signal (non-diffusion sensitized) with a *b*-value of 1200 and decimated to the desired resolution. Rician noise is added as

$$\widehat{\text{DWI}}_i \quad = \quad ||(\text{DWI}_i + n_R) + j(n_I)||_2 \tag{4.1}$$

$$n_R, n_I \quad \in \quad \mathcal{N}(0, \sigma = 1/SNR) \tag{4.2}$$

to get noisy $\widehat{\text{DWI}}_i$ from which the noisy diffusion tensors are computed. The geometries of phantom data are given in Figure 4.1.

For *in vivo* experiments, a diffusion weighted data set consisting of 17 volumes acquired with different gradient B-field directions (b = 800 s/mm^2), and one baseline volume acquired with no diffusion weighting (b = 0 s/mm^2) is used. The data were acquired using a Philips 3T whole-body scanner and a dual spin echo EPI imaging sequence. The images cover a field of view of 22.2 cm using a 128×128 grid. 60 image slices were acquired, with a slice thickness of 2 mm.
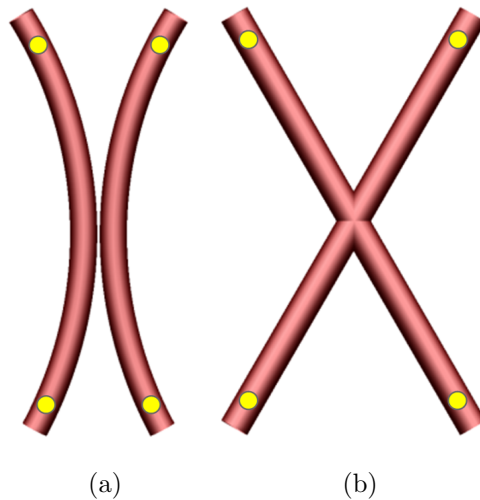
(a)   (b)

Figure 4.1. The two phantom geometries with the ROIs added on figures with yellow circles (a) Kissing (b) Crossing.

4.2. Evaluation Methodology

The quantitative evaluation is based on *sensitivity* (SN) and *false positive* (FP) rate measurements. Four cubic ROIs are chosen along the ground truth fibers. Figure 4.1 depicts the ground truth fibers used in phantom experiments and the ROIs. The selected (connected to the ones in the ROI) short tracts, that are determined with respect to the threshold T, are divided into two groups as inside and outside the ground truth fiber. The tracts that are partially inside the ground truth fibers are further divided into two. The insiders are projected onto the centerline of the ground truth fiber. SN is defined as the percentage of the ground truth centerline that is covered by the projected insiders, while FP rate is defined as the total length of the outsiders. Hence $1 > \text{SN} > 0$, and $\text{FP} \geq 0$. SN and FP rates are averaged over all ROIs for a single phantom. SN and FP rate are defined likewise for the standard long fiber tracts (streamline tracts), where each fiber is divided into two as inside and outside segment groups. The experiments are repeated for $SNR = \{8, 16, 24\}$ and resolutions $\{0.2^3, 0.4^3\}$ $unit^3$. As given above, resolution of the ground truth data is 0.1^3 $unit^3$, hence partial volume effect will be observed at resolutions 0.2^3 and 0.4^3 $unit^3$.

The qualitative evaluation is done by assessing the results for known fiber tract bundles at different thresholds (T). The ROIs were chosen on corpus callosum and

internal capsule. Resulting fiber tracts for the chosen ROIs are interpreted qualitatively based on known anatomical connections.

4.3. Experiments with Phantom DTI Data

As shown in Figure 4.1, each phantom geometry consists of two fibers. In kissing geometry, two fibers get close to each other in the middle without touching. However, due to partial volume effect, voxels at the center will be affected by both fibers in DTI data. In crossing geometry, two fibers cross in the middle, which will cause the tensors at the center to have ambiguous PDDs. The angle between the fibers is 60°.

In this section, figures from the tracking results for all SNR levels, all geometries and all resolutions will be given, for a single seed region. Following these figures, in Tables 4.1-4.4, numerical results are provided that are averaged over four ROIs as shown in Figure 4.1.

Figures 4.2-4.13 show the results of streamline tracking and the proposed approach for a single ROI. Tracts shown in red are the long fiber tracts that are generated using streamline tractography by taking every grid point within the ROI as a seed point. Tracts shown in green are the results of the proposed approach, and they form the set of short fiber tracts that are connected to the seed short tracts passing through the ROI, which is shown with a yellow circle, with a connectivity value higher than T. Two images are provided for each case, one for low T, and one for high T.

Figure 4.2. Outputs for kissing geometry at resolution 0.2^3 $unit^3$ and SNR = 8 (a) Streamline tracking (b) Proposed method at $T = 0$ (low) (c) Proposed method at $T = 5$ (high).

Figure 4.3. Outputs for kissing geometry at resolution 0.2^3 $unit^3$ and SNR = 16 (a) Streamline tracking (b) Proposed method at $T = 0$ (low) (c) Proposed method at $T = 5$ (high).

Figure 4.4. Outputs for kissing geometry at resolution $0.2^3 \ unit^3$ and SNR = 24 (a) Streamline tracking (b) Proposed method at $T = 0$ (low) (c) Proposed method at $T = 5$ (high).
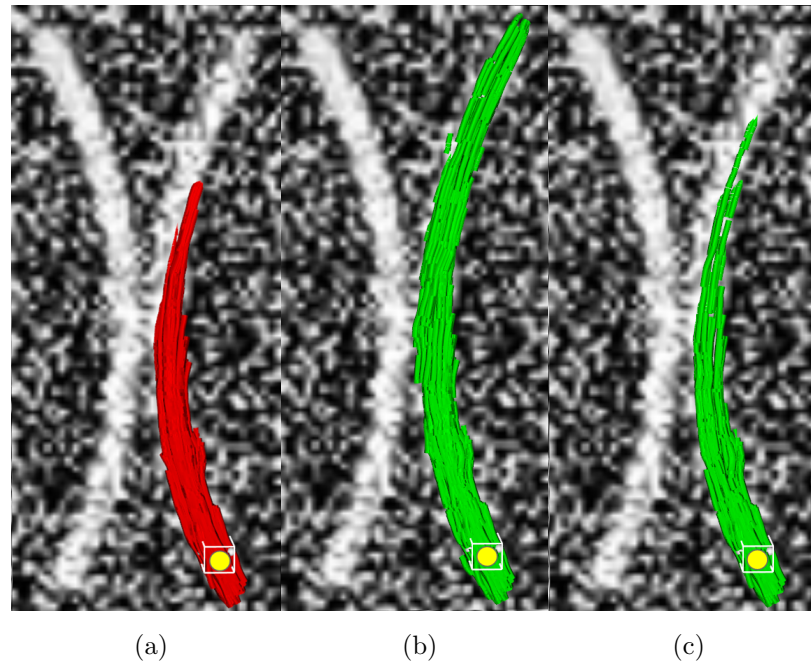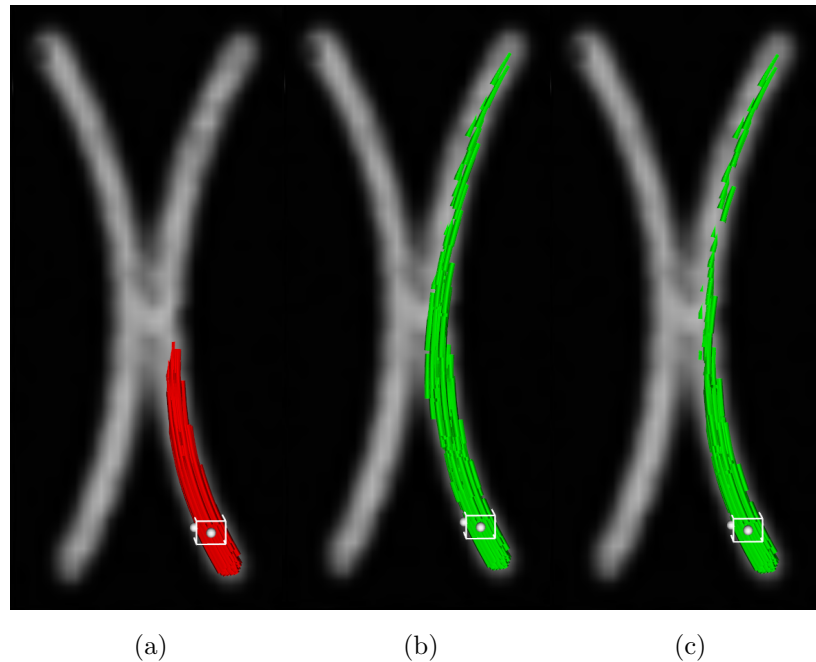

Figure 4.5. Outputs for kissing geometry at resolution $0.4^3 \ unit^3$ and SNR = 8 (a) Streamline tracking (b) Proposed method at $T = 0$ (low) (c) Proposed method at $T = 5$ (high).

(a)   (b)   (c)

Figure 4.6. Outputs for kissing geometry at resolution 0.4^3 $unit^3$ and SNR $= 16$ (a) Streamline tracking (b) Proposed method at $T = 0$ (low) (c) Proposed method at $T = 5$ (high).
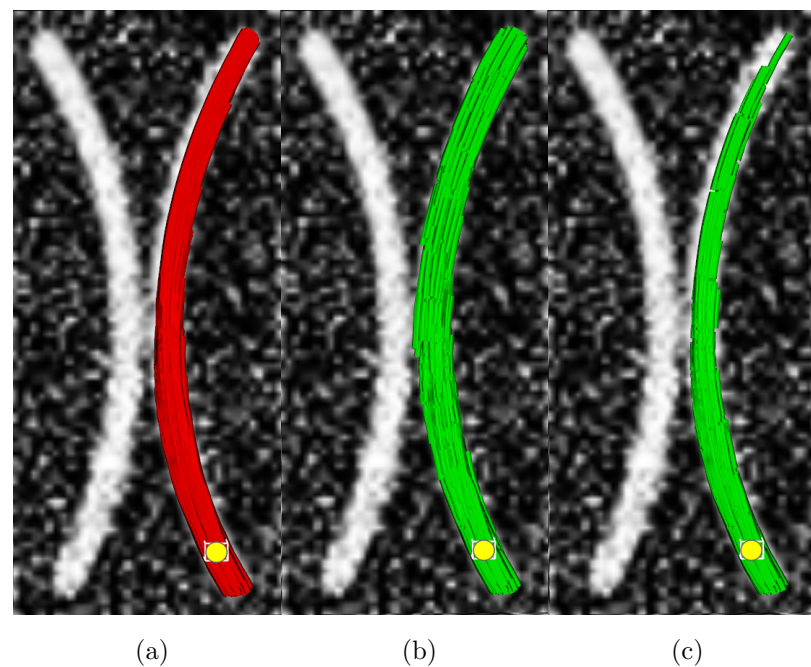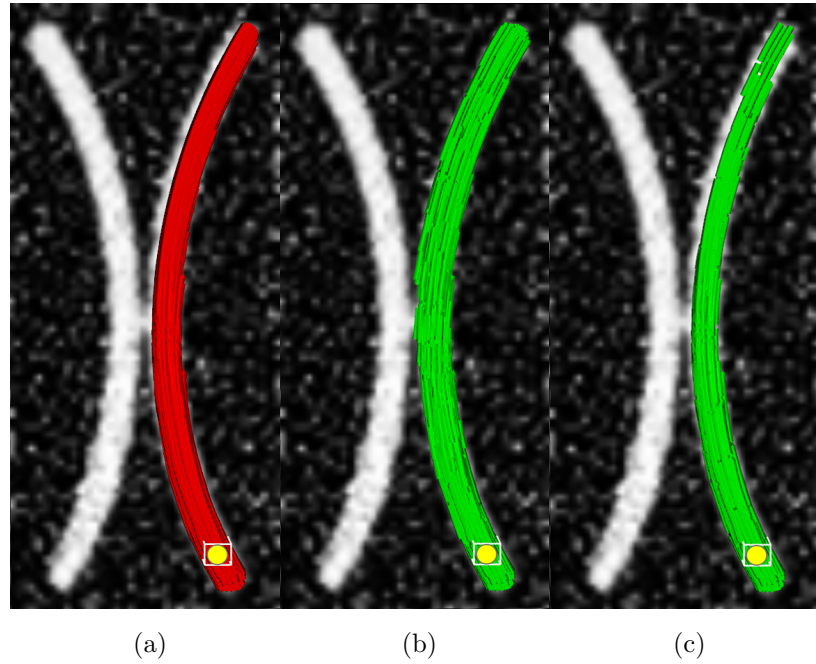

(a)   (b)   (c)

Figure 4.7. Outputs for kissing geometry at resolution 0.4^3 $unit^3$ and SNR $= 24$ (a) Streamline tracking (b) Proposed method at $T = 0$ (low) (c) Proposed method at $T = 5$ (high).
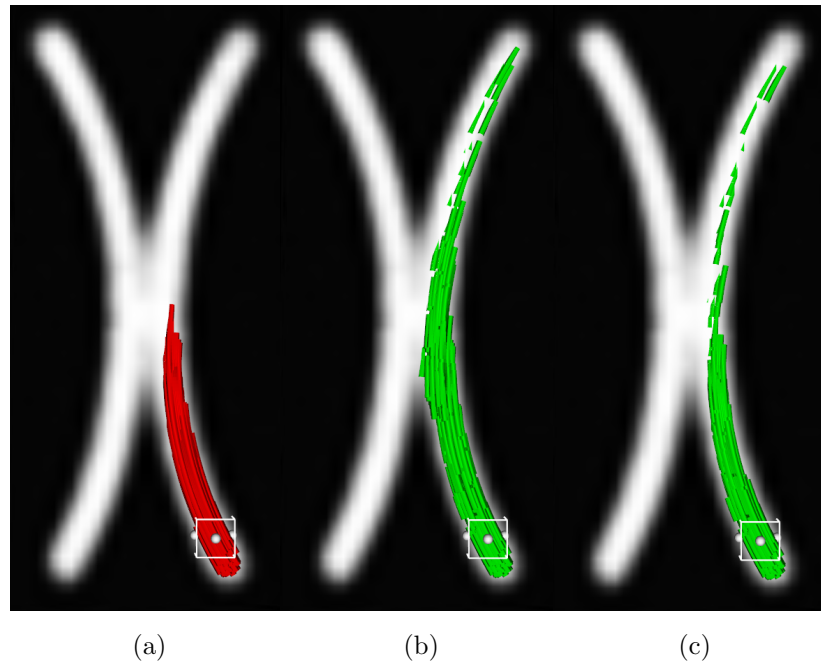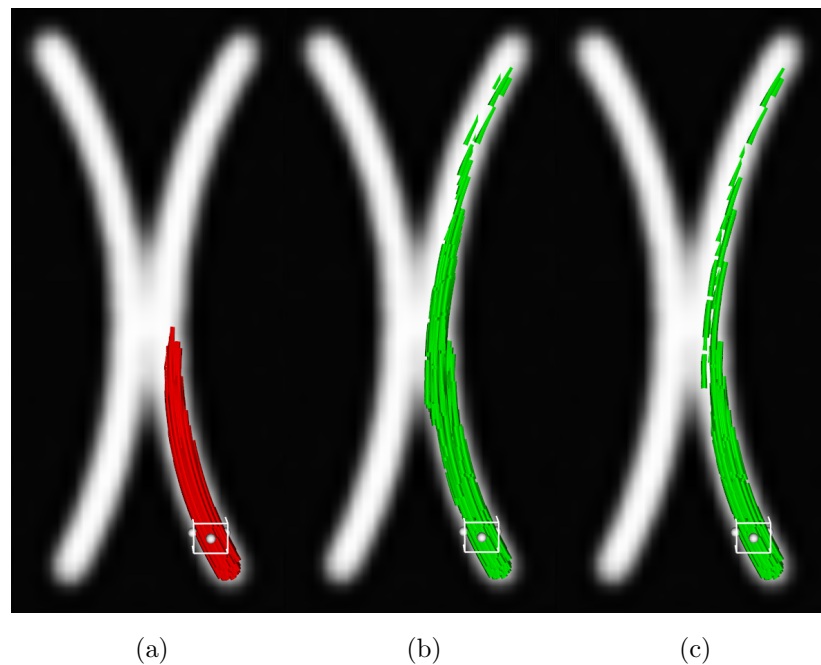
Figures 4.2-4.4 display the results for the kissing geometry for different SNR levels at resolution 0.2^3 $unit^3$. For SNR = {16, 24}, initial streamline tractography results are already true. Our approach fills in the fibers more solidly for low T, and show the more confident parts (fibers around the centerline) at high T. At SNR = 8, initial streamline tractography fails to follow the whole fiber. By creating bridges to the short fiber tracts that are close to the stopping point, our method is able to track the whole fiber successfully.

In Figures 4.5-4.7, results for kissing geometry at resolution 0.4^3 $unit^3$ are depicted. When compared to Figures 4.2-4.4, these figures are much more blurred due to a stronger partial volume effect. It can be also observed that, the fibers touch each other in the middle, even if the ground truth fibers do not. In all these SNR levels, streamline tracking ended prematurely without being able to track the whole fiber. In all cases, our method is able to force these results to track the whole fiber, without introducing any erroneous tracts.

Tables 4.1 and 4.2 give the quantitative evaluation results for kissing geometry at resolutions 0.2^3 $unit^3$ and 0.4^3 $unit^3$, using the methodology described in Section 4.2. First row in each table shows the performance (SN and FP rates) of streamline tractography with 4th order Runge-Kutta integration. Second row gives the performance of our method at the FP rate of streamline tractography, i.e., with no additional erroneous tracts. Last row shows the highest SN our method can achieve (low T), and the corresponding FP rate. From these tables, it can be seen that the proposed method improves the tracking results for all SNR and resolution levels. At resolution 0.2^3 $unit^3$ and SNR = {16, 24}, our method's tracking results are perfect, i.e., SN = 1 and FP = 0. For these cases, due to low noise and low partial volume effect, no ambiguity in DTI data is detected at the kissing point. This means, no single cluster starting from given seed ROIs has followed the wrong fiber. As expected, when voxel size is increased, performances of both streamline tracking and our method decrease. Still, our method has a marked advantage over streamline tracking.

Table 4.1. Quantitative evaluation results for kissing geometry at resolution $0.2^3\ unit^3$

	SNR = 8		SNR = 16		SNR = 24	
	Weighted histogram (SN / FP)	Bootstrap sampling (SN / FP)	Weighted histogram (SN / FP)	Bootstrap sampling (SN / FP)	Weighted histogram (SN / FP)	Bootstrap sampling (SN / FP)
Initial streamline tractography	0.10±0.14 / 0.00±0.00		0.19±0.29 / 0.00±0.00		0.23±0.29 / 0.00±0.00	
Proposed approach at FP rate of initial tractography	0.66±0.28/ 0.00±0.00	0.66±0.25/ 0.00±0.00	1.00±0.00/ 0.00±0.00	1.00±0.00/ 0.00±0.00	1.00±0.00/ 0.00±0.00	1.00±0.00/ 0.00±0.00
Proposed approach at highest SN	0.84±0.18/ 0.22±0.33	0.74±0.20/ 0.67±1.35	1.00±0.00/ 0.00±0.00	1.00±0.00/ 0.00±0.00	1.00±0.00/ 0.00±0.00	1.00±0.00/ 0.00±0.00

Table 4.2. Quantitative evaluation results for kissing geometry at resolution 0.4^3 $unit^3$

	SNR = 8		SNR = 16		SNR = 24	
	Weighted histogram (SN / FP)	Bootstrap sampling (SN / FP)	Weighted histogram (SN / FP)	Bootstrap sampling (SN / FP)	Weighted histogram (SN / FP)	Bootstrap sampling (SN / FP)
Initial streamline tractography	0.06±0.11 / 0.00±0.00		0.07±0.11 / 0.00±0.00		0.09±0.11 / 0.00±0.00	
Proposed approach at FP rate of initial tractography	0.57±0.26/ 0.00±0.00	0.60±0.25/ 0.00±0.00	0.73±0.23/ 0.00±0.00	0.70±0.27/ 0.00±0.00	0.64±0.24/ 0.00±0.00	0.63±0.23/ 0.00±0.00
Proposed approach at highest SN	0.64±0.22/ 1.25±2.30	0.64±0.22/ 1.25±2.30	0.75±0.26/ 3.2±6.4	0.71±0.28/ 1.87±3.75	0.75±0.24/ 4.00±8.00	0.74±0.23/ 2.82±5.65

Figure 4.8. Outputs for crossing geometry at resolution 0.2^3 $unit^3$ and SNR = 8 (a) Streamline tracking (b) Proposed method at $T = 0$ (low) (c) Proposed method at $T = 5$ (high).
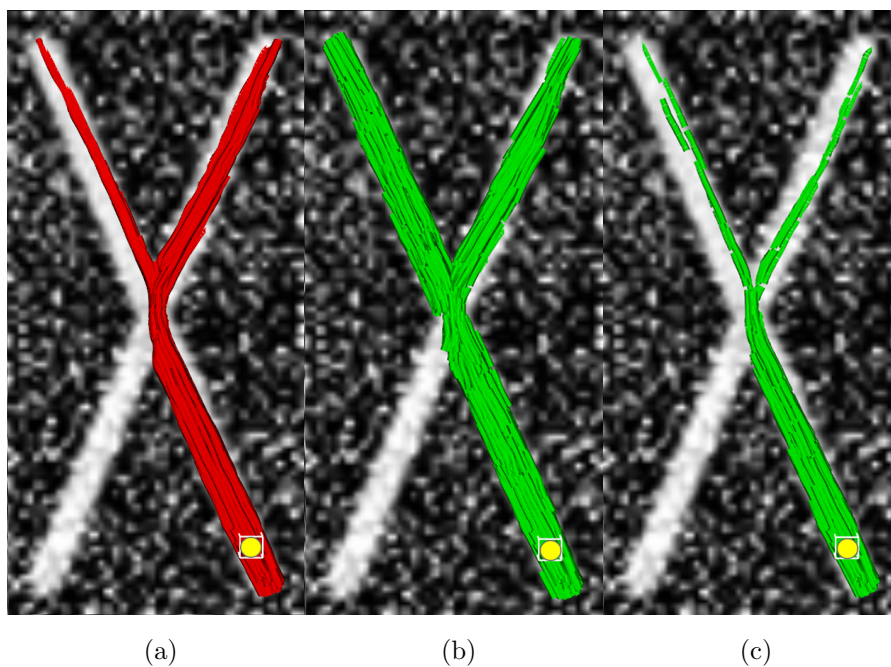
Figure 4.9. Outputs for crossing geometry at resolution 0.2^3 $unit^3$ and SNR = 16 (a) Streamline tracking (b) Proposed method at $T = 0$ (low) (c) Proposed method at $T = 5$ (high).

(a)   (b)   (c)
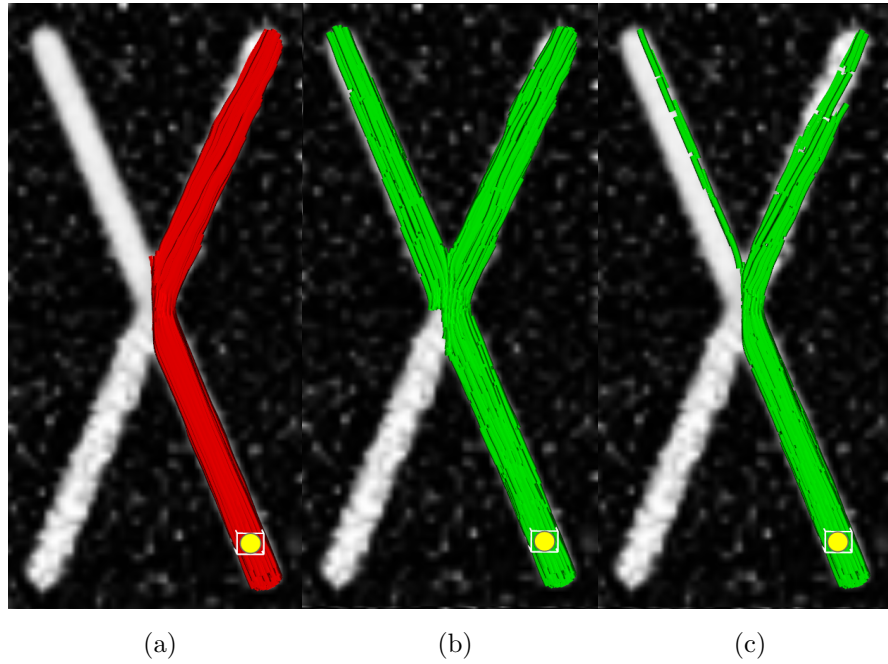
Figure 4.10. Outputs for crossing geometry at resolution $0.2^3 \ unit^3$ and SNR $= 24$ (a) Streamline tracking (b) Proposed method at $T = 0$ (low) (c) Proposed method at $T = 5$ (high).

(a)   (b)   (c)
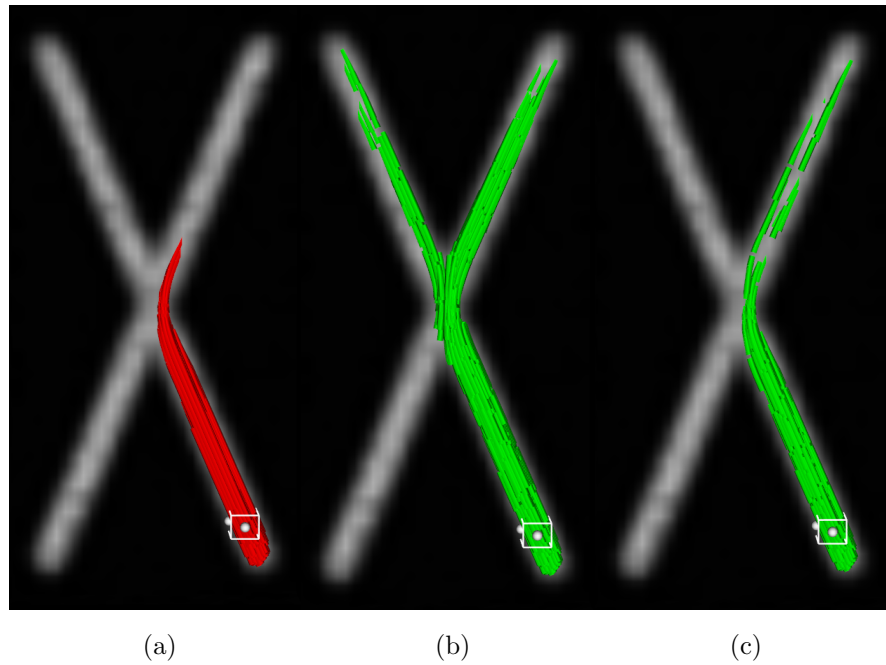
Figure 4.11. Outputs for crossing geometry at resolution $0.4^3 \ unit^3$ and SNR $= 8$ (a) Streamline tracking (b) Proposed method at $T = 0$ (low) (c) Proposed method at $T = 5$ (high).
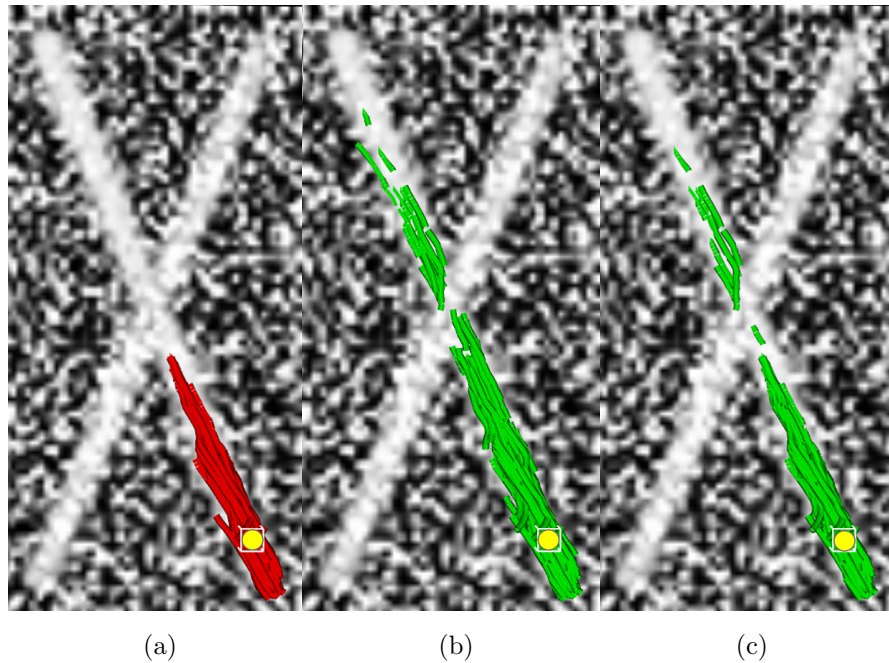
(a)　　　　　　　　　(b)　　　　　　　　　(c)

Figure 4.12. Outputs for crossing geometry at resolution 0.4^3 $unit^3$ and SNR $= 16$ (a) Streamline tracking (b) Proposed method at $T = 0$ (low) (c) Proposed method at $T = 5$ (high).

(a)　　　　　　　　　(b)　　　　　　　　　(c)

Figure 4.13. Outputs for crossing geometry at resolution 0.4^3 $unit^3$ and SNR $= 24$ (a) Streamline tracking (b) Proposed method at $T = 0$ (low) (c) Proposed method at $T = 5$ (high).

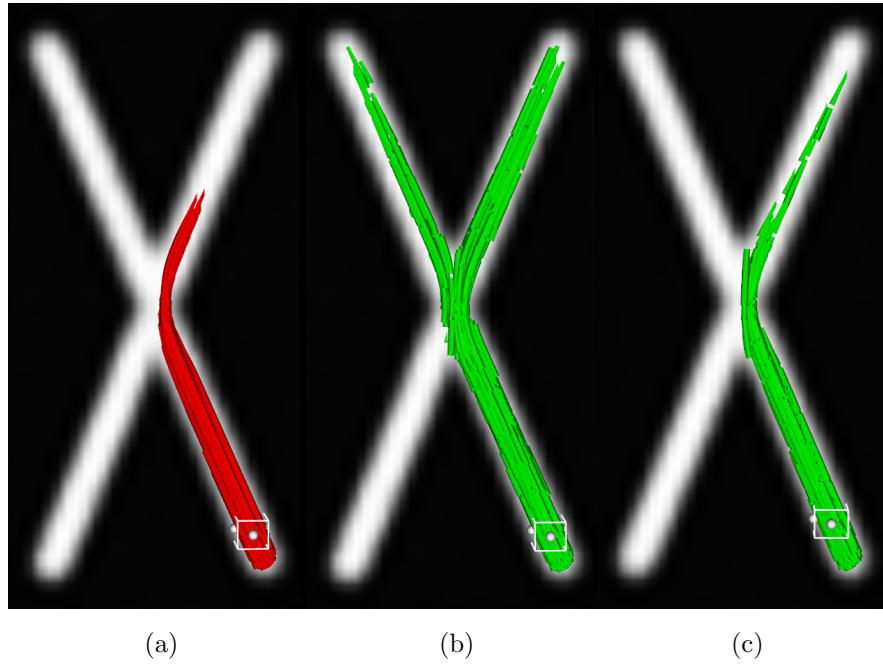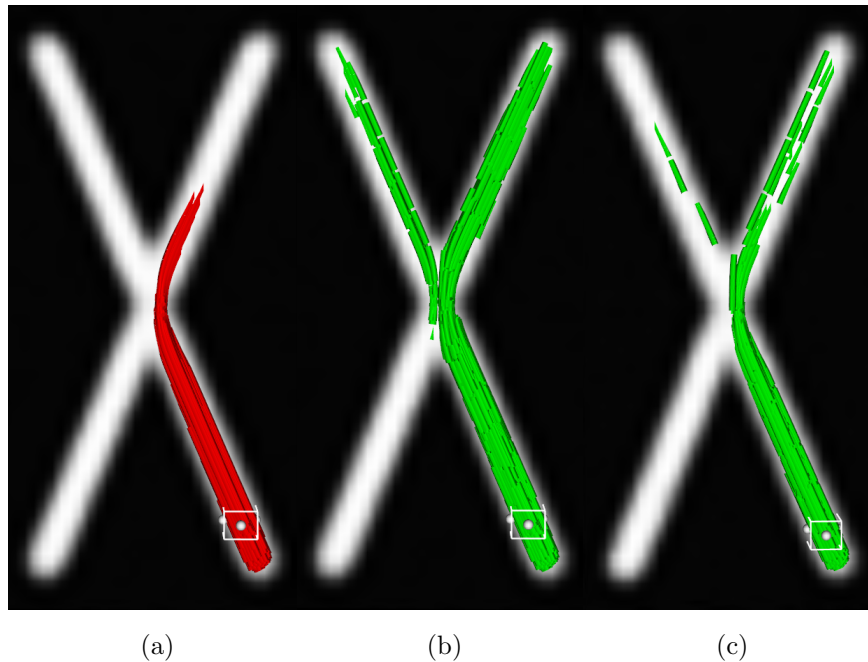Figures 4.8-4.10 illustrate the tracking results for the crossing geometry at resolution $0.2^3 \ unit^3$. Initial tractography fails to pass through the crossing point due to ambiguous PDD information for SNR = 8. Our method, on the other hand, completes most of the fiber via generating short tract clusters beyond the crossing point. For SNR = {16, 24}, the results demonstrate the proposed method's ability to highlight the problematic regions that correspond to high uncertainty in DTI data. For SNR = 24, all of the initial fibers (hence the base clusters) that are seeded from the points within the ROI follow the wrong direction at the crossing point. As stated in Chapter 1, our method is able to display the possible branching patterns of the fiber bundles. Figure 4.10 validates this statement, where the alternative path (which is actually true) is displayed along with the direction of initial tractography result, which is erroneous. However, Figures 4.9 and 4.10 also show that, when T is increased, our method has a tendency to favor the wrong direction, like streamline tractography. This is in line with the fact that, streamline tractography follows the most probable path, ignoring uncertainty in the data.

Example tracking results for the crossing geometry at resolution $0.4^3 \ unit^3$ are provided in Figures 4.11-4.13. In all of these results, streamline tractography fails at the crossing point, and follows the wrong fiber. Our method is shown to highlight the possible branching pattern. At SNR = {8, 16}, when T is increased, proposed method chooses the wrong direction, following the discussion above. At SNR = 24, even if T is increased, both directions are displayed.

Tables 4.3-4.4 give the numerical results for the crossing geometry. From these tables, FP rate of streamline tractography increases as SNR increases (See Figures 4.8-4.10). In this case, although our method is able to propose alternative paths (as observed from increased SN values), the FP rate of our method increases drastically. One reason for this is always sampling from the neighbourhood of base clusters. Another reason is that, FP rate is not normalized. Hence, populating this data with denser short tracts would result in an increased FP rate. The FP rates, however, should be interpreted conservatively as the total length of all outsider short tract segments contribute to it, even if they follow a single wrong path as in Figure 4.10.

Table 4.3. Quantitative evaluation results for crossing geometry at resolution $0.2^3\ unit^3$

	SNR = 8		SNR = 16		SNR = 24	
	Weighted histogram (SN / FP)	Bootstrap sampling (SN / FP)	Weighted histogram (SN / FP)	Bootstrap sampling (SN / FP)	Weighted histogram (SN / FP)	Bootstrap sampling (SN / FP)
Initial streamline tractography	0.09±0.09 / 0.00±0.00		0.18±0.15 / 0.87±1.75		0.22±0.07 / 1.52±1.98	
Proposed approach at FP rate of initial tractography	0.30±0.12/ 0.00±0.00	0.29±0.12/ 0.00±0.00	0.62±0.25/ 0.87±1.75	0.60±0.27/ 0.87±1.75	0.54±0.22/ 0.00±0.00	0.48±0.23/ 0.00±0.00
Proposed approach at highest SN	0.30±0.12/ 0.00±0.00	0.29±0.12/ 0.00±0.00	0.87±0.26/ 14.87±22.8	0.75±0.29/ 22.40±24.20	0.89±0.21/ 29.90±24.60	0.79±0.24/ 12.40±8.98

Table 4.4. Quantitative evaluation results for crossing geometry at resolution 0.4^3 $unit^3$

	SNR = 8		SNR = 16		SNR = 24	
	Weighted histogram (SN / FP)	Bootstrap sampling (SN / FP)	Weighted histogram (SN / FP)	Bootstrap sampling (SN / FP)	Weighted histogram (SN / FP)	Bootstrap sampling (SN / FP)
Initial streamline tractography	0.07±0.06 / 0.00±0.00		0.08±0.09 / 0.02±0.05		0.09±0.09 / 0.02±0.05	
Proposed approach at FP rate of initial tractography	0.21±0.19/ 0.00±0.00	0.21±0.20/ 0.00±0.00	0.41±0.15/ 0.02±0.05	0.39±0.12/ 0.02±0.05	0.46±0.12/ 0.02±0.05	0.42±0.14/ 0.02±0.05
Proposed approach at highest SN	0.21±0.19/ 0.00±0.00	0.21±0.20/ 0.00±0.00	0.75±0.21/ 7.27±8.03	0.67±0.19/ 5.70±6.69	0.58±0.01/ 4.05±3.69	0.58±0.01/ 5.30±5.76

The connectivity threshold T should be interpreted as a relative measure, which shows the confidence of the fiber tracts in a comparative manner. Hence, trying to find a global T value that would work for all cases is not sensible. Use of such a threshold provides user interactivity and it is the key to many of the virtues of the algorithm. If we see a significant change in the resulting short tract set by changing T, one should suspect about the reliability of the results of the initial tractography at the corresponding region. On the other hand, if T has no significant effect on the results, one can be confident about results of the initial tractography. Decreasing T will either increase the number of selected short tracts or will have no effect. At $T = 0$, all of the short tract clusters sampled from the set of base clusters will be displayed. All branching patterns, if any, will be observed at $T = 0$, and with increasing T, persistent branchings can be assessed.

From the results given in this section, the following facts can be inferred:

- With increasing SNR, performances of streamline tractography and the proposed method increase.
- With decreasing resolution (increasing voxel size), performances of streamline tractography and the proposed method decrease, as the partial volume effect becomes more prevalent.
- In all cases, our method achieves a higher SN value at the FP rate of streamline tractography.
- In most cases, weighted histogram sampling provides a slightly better performance compared to bootstrap sampling as the space of short tract clusters can be more thoroughly explored by generating a larger number of clusters. Yet, the computational cost of weighted histogram sampling is much higher.
- In some cases, performance of weighted histogram sampling is equal to that of bootstrap sampling. In such cases, no unseen cluster is present in the cluster set from which bootstrap samples are drawn. Clearly, using bootstrap sampling is advantageous in these cases due to its lower computational cost.

4.4. Experiments with Real DTI Data

As stated before, in addition to phantom experiments, the algorithm is tested on a healthy subject. Two ROIs are manually placed on anatomically well-known parts of the brain, namely, corpus callosum (colossal commissure) and internal capsule.

Firstly, a ROI is manually placed on corpus callosum on sagittal plane of the 3D view.
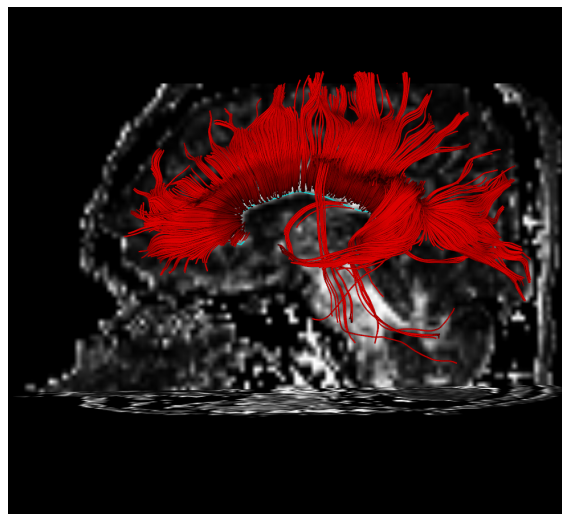
(a)
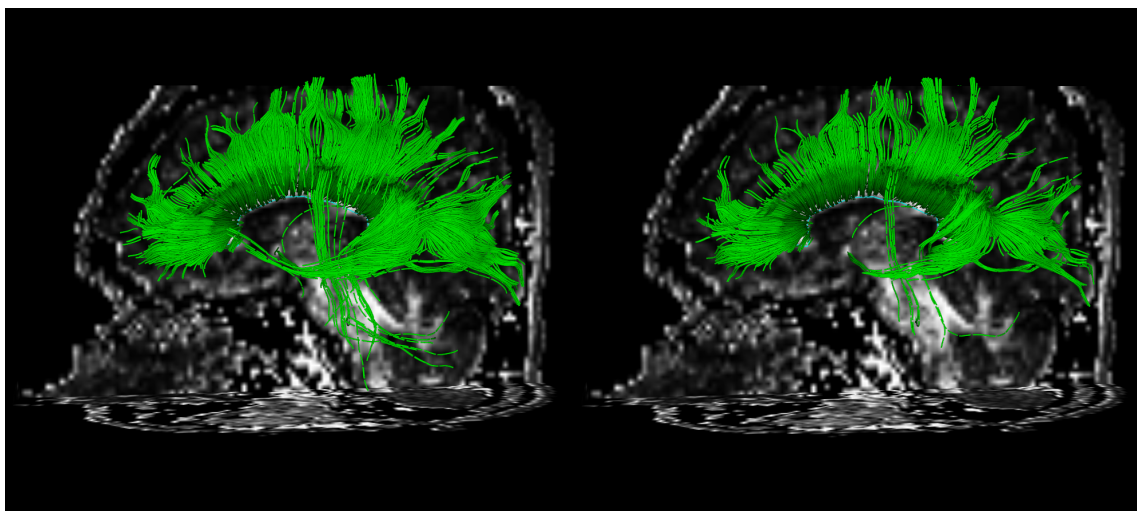
(b)   (c)

Figure 4.14. Outputs for a ROI placed on corpus callosum (a) Streamline tracking (b) Proposed method at $T = 0$ (low) (c) Proposed method at $T = 50$ (high).

Figure 4.14 (a) shows the result of streamline tracking for this region. From this figure, we can see that the fibers of corpus callosum are successfully found, however, parts of corticospinal tract, middle cerebellar peduncle and fornix are also erroneously tracked. At $T = 0$ (See Figure 4.14 (b)), the proposed approach also locates these incorrect tracts, along with fronto-occipital fascicle. However, it can be seen that in our method, the number of tracts along fornix are much less than streamline method. Figure 4.14 (c) shows the case where T is increased to 50. In this case, number of tracts along corticospinal tract, middle cerebellar peduncle and fronto-occipital fascicle considerably decreases, which shows that these tracts are not reliable.

Secondly, internal capsule, which consists of fiber bundles connecting the cerebral cortex and the pyramids of the medulla, is inspected. A ROI is manually placed on posterior segment of internal capsule on axial plane of the 3D view. From Figure 4.15 (a), we can see that streamline tractography has erroneous connections to middle cerebellar peduncle and corpus callosum. Moreover, there are connections to the wrong hemisphere of the brain. Result of the proposed method is similar to that of streamline tractography at $T = 0$, as shown in Figure 4.15 (b). When T is increased to 100, we see that almost all of these errors are successfully eliminated, which can be observed in Figure 4.15 (c). The results given in Figures 4.14 and 4.15 confirm that our method can correctly assign relative confidence to fibers in the given tractography results. By changing T, erroneous tracts can be eliminated from given results.
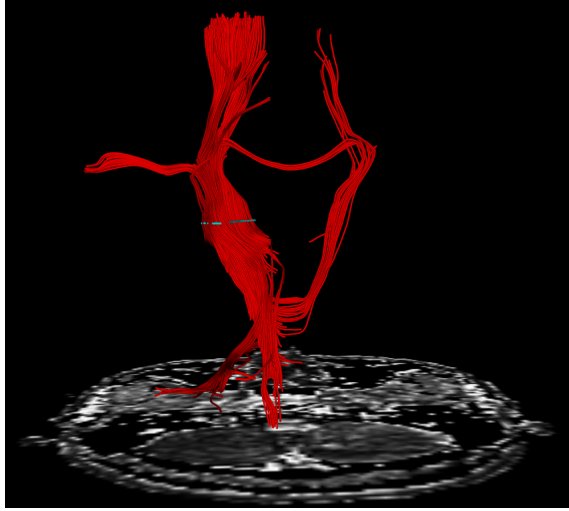
(a)
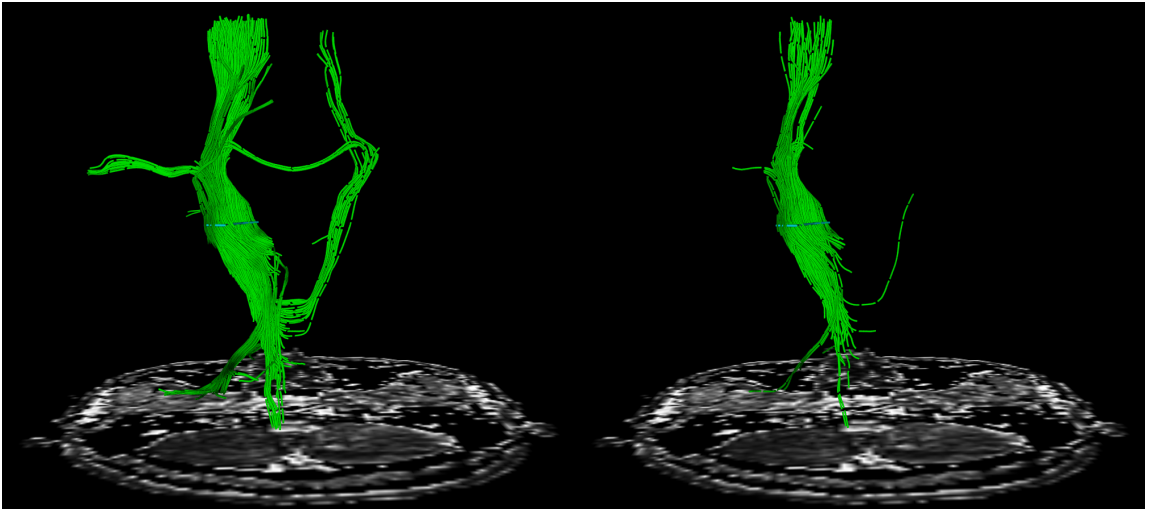
(b)   (c)

Figure 4.15. Outputs for a ROI placed on internal capsule (a) Streamline tracking (b)

Proposed method at $T = 0$ (low) (c) Proposed method at $T = 100$ (high).

5. CONCLUSION

In this thesis, a white matter tractography assessment and improvement method that relies on sampling the short fiber clusters has been proposed. The proposed method combines easy comprehensibility of deterministic tractography methods and fidelity of probabilistic methods to DTI data. The method takes a set of tracts as its input and assesses the given results via

- Assigning relative confidence to fibers
- Highlighting erroneous/uncertain regions
- Introducing alternative paths

where the input tracts may be generated with any tractography algorithm.

For a given seed region, the result of the technique is a set of short tracts, which can be filtered interactively by changing the connectivity threshold to the selected set of seed short tracts. This allows the user to inspect the unreliable regions in the initial tractography results and to see possible branching patterns in real time.

The proposed method is evaluated quantitatively on phantom and qualitatively on real DTI data. For both cases, input tracts are generated with streamline tractography with 4th order Runge-Kutta numerical integration algorithm [25]. In quantitative experiments, it is observed that, the proposed method successfully highlights the uncertainties in the DTI data, and suggests alternative paths at such regions. Streamline tracking, on the other hand, masks these regions by selecting a single direction. Moreover, quantitative experiments show that the proposed method consistently improves tracking results in all cases (different fiber geometries, SNR values and resolutions) compared to streamline tractography. It is also shown that, the method can solve the kissing and crossing fiber problem.

In qualitative experiments, two of the anatomically well-known regions of brain are inspected, which are corpus callosum and internal capsule. It is observed, the proposed method can successfully generate anatomically sound fiber tracts. It is also shown that, the erroneous connections in input tracts can be eliminated by increasing the connectivity threshold.

The major drawback of the method is its high computational cost, like all probabilistic tractography methods. Using bootstrap sampling reduces the computation time, at the expense of not being able to explore the short tract cluster fully. However the computations are done once for a dataset and interactive assessment can be performed in real time.

Among future prospects, using multiple ROIs stands out as the first extension. When multiple ROIs are defined, one can use boolean operators to display the fibers that pass through all or at least one of these ROIs. When the fibers that pass through all ROIs are displayed, the outlier tracts can be eliminated. When the fibers passing through at least one of these ROIs are displayed, several regions of brain can be analyzed simultaneously. More importantly, another extension is combining DTI with functional magnetic resonance imaging (fMRI). fMRI represents the gray matter activation, which is the neuronal population response to a specific task. While DTI can be used to study anatomical architecture of human brain, fMRI provides information about functional architecture of the brain *in vivo*. As pointed out in Chapter 1, DTI is widely used in presurgical planning. Combining fMRI data in the planning step, a surgeon can change or enhance the course of treatment. Ultimately, combining these two types of information can allow us to better understand the organization and dynamics of neural systems in human brain, and consequently neural functions and human behavior.

REFERENCES

1. Basser, P. J., J. Mattiello and D. L. Bihan, "Estimation of The Effective Self-Diffusion Tensor from the NMR Spin Echo", *Journal of Magnetic Resonance, Series B*, Vol. 103, No. 3, pp. 247–254, 1994.

2. Basser, P. J., "Inferring Microstructural Features and the Physiological State of Tissues from Diffusion-Weighted Images", *NMR in Biomedicine*, Vol. 8, No. 7-8, pp. 333–344, 1995.

3. Basser, P. J. and C. Pierpaoli, "Microstructural and Physiological Features of Tissues Elucidated by Quantitative Diffusion Tensor MRI", *Journal of Magnetic Resonance, Series B*, Vol. 111, No. 3, pp. 209–219, 1996.

4. Assaf, Y. and O. Pasternak, "Diffusion Tensor Imaging (DTI)-Based White Matter Mapping in Brain Research: A Review", *Journal of Molecular Neuroscience*, Vol. 34, No. 1, pp. 51–61, 2008.

5. Lazar, M., "Mapping Brain Anatomical Connectivity Using White Matter Tractography", *NMR in Biomedicine*, Vol. 23, No. 7, pp. 821–835, 2010.

6. Rollins, N. K., "Clinical Applications of Diffusion Tensor Imaging and Tractography in Children", *Pediatric Radiology*, Vol. 37, No. 8, pp. 769–780, 2007.

7. Price, G., M. Cercignani, G. J. M. Parker, D. R. Altmann, T. R. E. Barnes, G. J. Barker, E. M. Joyce and M. A. Ron, "White Matter Tracts in First-Episode Psychosis: A DTI Tractography Study of the Uncinate Fasciculus", *Neuroimage*, Vol. 39, No. 3, pp. 949–955, 2008.

8. Schonberg, T., P. Pianka, T. Hendler, O. Pasternak and Y. Assaf, "Characterization of Displaced White Matter by Brain Tumors Using Combined DTI and fMRI", *Neuroimage*, Vol. 30, No. 4, pp. 1100–1111, 2006.

9. Mori, S. and P. C. M. V. Zijl, "Fiber Tracking: Principles and Strategies - A Technical Review", *NMR in Biomedicine*, Vol. 15, No. 7-8, pp. 468–480, 2002.

10. Bozkaya, U. and B. Acar, "SMT: Split/Merge Fiber Tractography for DT-MRI", *Proceedings of the International Conference on Medical Image Computing and Computer-Assisted Intervention*, pp. 153–160, Brisbane, Australia, 2007.

11. Wong, C. W., *Diffusion MRI White Matter Tractography: Estimation of Multiple Fibers per Voxel Using Independent Component Analysis*, Ph.D. Thesis, University of Southern California, 2009.

12. Morris, C. G. and A. A. Maisto, *Psychology: An Introduction*, Prentice Hall, 11th edition, 2001.

13. Bammer, R., B. Acar and M. E. Moseley, "In Vivo MR Tractography Using Diffusion Imaging", *European Journal of Radiology*, Vol. 45, No. 3, pp. 223–234, 2003.

14. Borisenko, A. I. and I. E. Tarapov, *Vector and Tensor Analysis with Applications*, Dover Publications, Inc., 1979.

15. Behrens, T., *MR Diffusion Tractography: Methods and Applications*, Ph.D. Thesis, University of Oxford, 2004.

16. Kingsley, P. B., "Introduction to Diffusion Tensor Imaging Mathematics: Part II. Anisotropy, Diffusion-Weighting Factors, and Gradient Encoding Schemes", *Concepts in Magnetic Resonance*, Vol. 28A, No. 2, pp. 123–154, 2006.

17. Kingsley, P. B., "Introduction to Diffusion Tensor Imaging Mathematics: Part III. Tensor Calculation, Noise, Simulations, and Optimization", *Concepts in Magnetic Resonance*, Vol. 28A, No. 2, pp. 155–179, 2006.

18. Taylor, A. J., *Diffusion Tensor Imaging: Evaluation of Tractography Algorithm Performance Using Ground Truth Phantoms*, M.S. Thesis, Virginia Polytechnic Institute and State University, 2004.

19. Dougherty, G., "Image Analysis in Medical Imaging: Recent Advances in Selected Examples", *Biomedical Imaging and Intervention Journal*, Vol. 6, No. 3, p. e32, 2010.

20. Bihan, D. L., J.-F. Mangin, C. Poupon, C. A. Clark, S. Pappata, N. Molko and H. Chabriat, "Diffusion Tensor Imaging: Concepts and Applications", *Journal of Magnetic Resonance Imaging*, Vol. 13, No. 4, pp. 534–546, 2001.

21. Lin, C.-P., W.-Y. I. Tseng, H.-C. Cheng and J.-H. Chen, "Validation of Diffusion Tensor Magnetic Resonance Axonal Fiber Imaging with Registered Manganese-Enhanced Optic Tracts", *Neuroimage*, Vol. 14, No. 5, pp. 1035–1047, 2001.

22. Basser, P. J., S. Pajevic, C. Pierpaoli, J. Duda and A. Aldroubi, "In Vivo Fiber Tractography Using DT-MRI Data", *Magnetic Resonance in Medicine*, Vol. 44, No. 4, pp. 625–632, 2000.

23. Conturo, T., N. Lori, T. Cull, E. Akbudak, A. Snyder, J. Shimony, R. McKinstry, H. Burton and M. Raichle, "Tracking Neuronal Fiber Pathways in the Living Human Brain", *Proceedings of the National Academy of Sciences of the United States of America*, Vol. 96, No. 18, pp. 10422–10427, 1999.

24. Mori, S., B. J. Crain, V. P. Chacko and P. C. M. V. Zijl, "Three Dimensional Tracking of Axonal Projections in the Brain by Magnetic Resonance Imaging", *Annals of Neurology*, Vol. 45, No. 2, pp. 265–269, 1999.

25. Tench, C. R., P. S. Morgan, M. Wilson and L. D. Blumhardt, "White Matter Mapping Using Diffusion Tensor MRI", *Magnetic Resonance in Medicine*, Vol. 47, No. 5, pp. 967–972, 2002.

26. Jones, D., A. Simmons, S. Williams and M. Horsfield, "Non-Invasive Assessment of Axonal Fiber Connectivity in the Human Brain via Diffusion Tensor MRI", *Magnetic Resonance in Medicine*, Vol. 42, No. 1, pp. 37–41, 1999.

27. Lazar, M., D. M. Weinstein, J. S. Tsuruda, K. M. Hasan, K. Arfanakis, M. E. Meyerand, B. Badie, H. A. Rowley, V. Haughton, A. Field and A. L. Alexander, "White Matter Tractography Using Diffusion Tensor Deflection", *Human Brain Mapping*, Vol. 18, No. 4, pp. 306–321, 2003.

28. Weinstein, D., G. Kindlmann and E. Lundberg, "Tensorlines: Advection-Diffusion Based Propagation Through Diffusion Tensor Fields", *Proceedings of the Conference on Visualization*, pp. 249–253, 1999.

29. Yoruk, E. and B. Acar, "Structure Preserving Regularization of DT-MRI Vector Fields by Nonlinear Anisotropic Diffusion Filtering", *Proceedings of the 13th European Signal Processing Conference*, Antalya, Turkey, 2005.

30. Clarke, R. A., P. Scifo, G. Rizzo, F. Dell'Acqua, G. Scotti and F. Fazio, "Noise Correction on Rician Distributed Data for Fibre Orientation Estimators", *IEEE Transactions on Medical Imaging*, Vol. 27, No. 9, pp. 1242–1251, 2008.

31. Martin-Fernandez, M., E. Munoz-Moreno, L. Cammoun, J.-P. Thiran, C.-F. Westin and C. Alberola-Lopez, "Sequential Anisotropic Multichannel Wiener Filtering with Rician Bias Correction Applied to 3D Regularization of DWI Data", *Medical Image Analysis*, Vol. 13, No. 1, pp. 19–35, 2009.

32. Yamada, K., K. Sakai, K. Akazawa, S. Yuen and T. Nishimura, "MR Tractography: A Review of Its Clinical Applications", *Magnetic Resonance in Medical Sciences*, Vol. 8, No. 4, pp. 165–174, 2009.

33. Lazar, M. and A. L. Alexander, "White Matter Tractography Using Random Vector (RAVE) Perturbation", *Proceedings of the International Society of Magnetic Resonance in Medicine*, p. 539, 2002.

34. Parker, G. J., H. A. Haroon and C. A. Wheeler-Kingshott, "A Framework for a Streamline-Based Probabilistic Index of Connectivity (PICo) Using a Structural Interpretation of MRI Diffusion Measurements", *Journal of Magnetic Resonance*

Imaging, Vol. 18, No. 2, pp. 242–254, 2003.

35. Behrens, T. E. J., M. W. Woolrich, M. Jenkinson, H. Johansen-Berg, R. G. Nunes, S. Clare, P. M. Matthews, J. M. Brady and S. M. Smith, "Characterization and Propagation of Uncertainty in Diffusion-Weighted MR Imaging", *Magnetic Resonance in Medicine*, Vol. 50, No. 5, pp. 1077–1088, 2003.

36. Friman, O., G. Farneback and C.-F. Westin, "A Bayesian Approach for Stochastic White Matter Tractography", *IEEE Transactions on Medical Imaging*, Vol. 25, No. 8, pp. 965–978, 2006.

37. Behrens, T. E. J., H. J. Berg, S. Jbabdi, M. F. Rushworth and M. W. Woolrich, "Probabilistic Diffusion Tractography with Multiple Fibre Orientations: What can We Gain?", *Neuroimage*, Vol. 34, No. 1, pp. 144–155, 2007.

38. Cook, P. A., D. C. Alexander and G. J. M. Parker, "Modelling Noise-Induced Fibre-Orientation Error in Diffusion-Tensor MRI", *Proceedings of the IEEE International Symposium on Biomedical Imaging*, pp. 332–335, 2004.

39. Sherbondy, A. J., R. F. Dougherty, M. Ben-Shachar, S. Napel and B. A. Wandell, "ConTrack: Finding the Most Likely Pathways Between Brain Regions Using Diffusion Tractography", *Journal of Vision*, Vol. 8, No. 9, pp. 1–16, 2008.

40. Koch, M. A., D. G. Norris and M. Hund-Georgiadis, "An Investigation of Functional and Anatomical Connectivity Using Magnetic Resonance Imaging", *Neuroimage*, Vol. 16, No. 1, pp. 241–250, 2002.

41. Hagmann, P., J. P. Thiran, L. Jonasson, P. Vandergheynst, S. Clarke, P. Maeder and R. Meuli, "DTI Mapping of Human Brain Connectivity: Statistical Fibre Tracking and Virtual Dissection", *Neuroimage*, Vol. 19, No. 3, pp. 545–554, 2003.

42. Lazar, M. and A. L. Alexander, "Bootstrap White Matter Tractography (BOOT-TRAC)", *Neuroimage*, Vol. 24, No. 2, pp. 524–532, 2005.

43. Efron, B., "Bootstrap Methods: Another Look at the Jackknife", *The Annals of Statistics*, Vol. 7, No. 1, pp. 1–26, 1979.

44. O'Gorman, R. L. and D. K. Jones, "Just How Much Data Need to Be Collected for Reliable Bootstrap DT-MRI?", *Magnetic Resonance in Medicine*, Vol. 56, No. 4, pp. 884–890, 2006.

45. Jones, D. K., "Tractography Gone Wild: Probabilistic Fibre Tracking Using the Wild Bootstrap with Diffusion Tensor MRI", *IEEE Transactions on Medical Imaging*, Vol. 27, No. 9, pp. 1268–1274, 2008.

46. Berman, J. I., S. Chung, P. Mukherjee, C. P. Hess, E. T. Han and R. G. Henry, "Probabilistic Streamline Q-Ball Tractography Using the Residual Bootstrap", *Neuroimage*, Vol. 39, No. 1, pp. 215–222, 2008.

47. Yuan, Y., H. Zhu, J. G. Ibrahim, W. Lin and B. S. Peterson, "A Note on the Validity of Statistical Bootstrapping for Estimating the Uncertainty of Tensor Parameters in Diffusion Tensor Images", *IEEE Transactions on Medical Imaging*, Vol. 27, No. 10, pp. 1506–1514, 2008.

48. Morris, D. M., K. V. Embleton and G. J. M. Parker, "Probabilistic Fibre Tracking: Differentiation of Connections from Chance Events", *Neuroimage*, Vol. 42, No. 4, pp. 1329–1339, 2008.

49. Arsigny, V., P. Fillard, X. Pennec and N. Ayache, "Log-Euclidean Metrics for Fast and Simple Calculus on Diffusion Tensors", *Magnetic Resonance in Medicine*, Vol. 56, No. 2, pp. 411–421, 2006.

50. Acar, B., R. Bammer and M. E. Moseley, "Comparative Assessment of DT-MRI Fiber Tractography Algorithms", *Proceedings of the International Society of Magnetic Resonance in Medicine*, p. 2164, Toronto, Canada, 2003.